AGU PUBLICATIONS

JGR

Journal of Geophysical Research: Solid Earth

RESEARCH ARTICLE
10.1002/2017JB015354

Key Points:
- Heterogeneous domain of elastic fault model alters the prediction of seafloor deformation and tsunamis
- Trench-breaking boundary condition of geodetic inverse analysis controls the resolved seismic and tsunami sources
- Finite element deformation models account for realistic slab curvature, bathymetry, and tomography-based crustal material distribution

Supporting Information:
- Supporting Information S1
- Table S1
- Table S2
- Table S3

Correspondence to:
S. Tung,
sui.tung@sdsmt.edu

Citation:
Tung, S., & Masterlark, T. (2018). Sensitivities of near-field tsunami forecasts to megathrust deformation predictions. *Journal of Geophysical Research: Solid Earth*, *123*, 1711–1735. https://doi.org/10.1002/2017JB015354

Received 13 DEC 2017
Accepted 2 FEB 2018
Accepted article online 12 FEB 2018
Published online 26 FEB 2018

Sensitivities of Near-field Tsunami Forecasts to Megathrust Deformation Predictions

S. Tung[1] **and T. Masterlark**[1]

[1]Department of Geology and Geological Engineering, South Dakota School of Mines and Technology, Rapid City, SD, USA

Abstract This study reveals how modeling configurations of forward and inverse analyses of coseismic deformation data influence the estimations of seismic and tsunami sources. We illuminate how the predictions of near-field tsunami change when (1) a heterogeneous (HET) distribution of crustal material is introduced to the elastic dislocation model, and (2) the near-trench rupture is either encouraged or suppressed to invert spontaneous coseismic displacements. Hypothetical scenarios of megathrust earthquakes are studied with synthetic Global Positioning System displacements in Cascadia. Finite-element models are designed to mimic the subsurface heterogeneity across the curved subduction margin. The HET lithospheric domain modifies the seafloor displacement field and alters tsunami predictions from those of a homogeneous (HOM) crust. Uncertainties persist as the inverse analyses of geodetic data produce nonrealistic slip artifacts over the HOM domain, which propagates into the prediction errors of subsequent tsunami arrival and amplitudes. A stochastic analysis further shows that the uncertainties of seismic tomography models do not degrade the solution accuracy of HET over HOM. Whether the source ruptures near the trench also controls the details of the seafloor disturbance. Deeper subsurface slips induce more seafloor uplift near the coast and cause an earlier arrival of tsunami waves than surface-slipping events. We suggest using the solutions of zero-updip-slip and zero-updip-slip-gradient rupture boundary conditions as end-members to constrain the tsunami behavior for forecasting purposes. The findings are important for the near-field tsunami warning that primarily relies on the near-real-time geodetic or seismic data for source calibration before megawaves hit the nearest shore upon tsunamigenic events.

1. Introduction

The time series of tsunami wave propagation are usually computed from the spontaneous changes of seafloor condition to forecast the coastal inundation and runups (Satake, 2014; Synolakis, 2003; Titov & Gonzalez, 1997; Wang & Power, 2011). The abrupt seafloor deformation can be calculated from the coseismic slip distributions which are the products of the inverse analyses of near-field tsunamic (Satake et al., 2013), seismological (e.g., W-Phase and centroid moment tensor) (Yamazaki et al., 2013), or geodetic (e.g., Global Positioning System [GPS]) (Ohta et al., 2012) measurements. Current modeling techniques used to develop inundation maps and evacuation plans typically rely on homogeneous (HOM), elastic, half-space dislocation solutions (e.g., Okada, 1985) to simulate slip-induced deformation (Fujii & Satake, 2007; Goda et al., 2014; Wei et al., 2014). While such analytical solutions are computationally efficient, they overly simplify the mechanically complex structure of upper crust along plate margins (Bjarnason et al., 1993; Gutscher et al., 2000)—a problem which translates to prediction errors for the seafloor deformation that drives tsunami genesis (Wei et al., 2014). A wide range of studies have already revealed the influence of subsurface rock heterogeneity in deriving coseismic rupture characteristics (Eleonora et al., 2002; Fernandez et al., 1996; He & Peltzer, 2009; He et al., 2003; Hughes et al., 2010; Jovanovich et al., 1974; Kyriakopoulos et al., 2013; Masterlark et al., 2001; Masterlark et al., 2012; Pan, 1999; Sato, 1971; Savage, 1987, 1998; Trasatti et al., 2011; Tung & Masterlark, 2016, 2018; Wang et al., 2006), when inverting the earthquake deformation recorded by GPS and interferometric synthetic aperture radar data. Therefore, we propose to investigate whether the distributed rock properties in deformational models might become significant enough to alter the predictions of seafloor deformation and subsequent tsunami behavior.

It is accepted that good compatibility between the deformational model assumptions and the realistic structural/lithospheric settings shape the interpretation of retrieved seismic information (Menke, 2012). Given a particular slip distribution, the forward models of half-space solutions usually underestimate and overestimate displacements over weak and rigid zones, respectively (Kyriakopoulos et al., 2013; Masterlark et al., 2001; Tung & Masterlark, 2016). From a forecasting standpoint, these uncertainties of estimated

seafloor movements essentially propagate into tsunami modeling and degenerate the fidelity of tsunami predictions (Goda et al., 2014; Wei et al., 2014). The prediction errors are expected to be larger especially near subduction zones where the distinctive material contrast between the denser oceanic and less-dense continental plate further deviates from the assumption of a HOM crust (Calvert et al., 2011; Kim et al., 2014). In this study, we build finite element deformation models (FEMs) to mimic the realistic lithospheric domain based on the CRUST 2.0 velocity model (Bassin et al., 2000) (Figure 2), from which the subsurface rock heterogeneity is simulated (Masterlark et al., 2012, 2016). By inspecting the seafloor deformation signatures of megathrust earthquake scenarios, we investigate the sensitivities of estimated tsunami waveforms to the different distributions of crustal materials within elastic forward models. We test the hypothesis that different configurations of crustal domains lead to various signatures of seafloor deformation and hence near-field tsunami impacts.

The modeled tsunami wave profiles are sensitive to earthquake slip patterns by which a tsunami is triggered. Ulutas (2013) compared the tsunami prediction from a uniform slip against a nonuniform slip, while Goda et al. (2014) performed a stochastic analysis among random-field slip models for the 2011 Tohoku earthquake, both suggesting discernible tsunami-slip sensitivity. The details of rupturing location and magnitude are critical to the computations of near-field tsunami impact (González et al., 2009; Priest et al., 2010; Yamazaki et al., 2013) but relatively insensitive to the far-field estimation (Okal & Synolakis, 2008; Titov et al., 1999). For megathrust events along subduction zones, rupture of the trench axis governs the overall patterns of tsunami amplitude and wavelength, resulting in the distinct extent of inundation and runup (Fujii et al., 2011; Uslu et al., 2007). Within the context of the earthquake-source inversions having smoothing or regularization, the slip solution is subject to boundary conditions that constrain the rupture to either propagate updip to or diminish near the trench (Menke, 2012). Taking the 2011 Tohoku event as an example, a variety of existing slip models from tsunami, seismological, and geodetic data show either primary trench breaking (Grilli et al., 2013; Gusman et al., 2012; Iinuma et al., 2012; Kyriakopoulos et al., 2013; Satake et al., 2013; Shao et al., 2011; Wei et al., 2014; Yamazaki et al., 2013; Yue & Lay, 2011) or dominated subsurface rupture (Ammon et al., 2011; Hayes, 2011; Iinuma et al., 2011; Lee, 2012; Ozawa et al., 2011; Romano et al., 2014; Shao et al., 2011; Simons et al., 2011; Suito et al., 2012). Unlike those inland earthquakes, the real-time detection of trench-breaking rupture is particularly challenging for submarine seismicity along subduction zones, as the seafloor rupture is difficult to be observed with remote geophysical instruments, even if there is good coverage of seafloor benchmarks or optical fiber networks (Fujihashi et al., 2007; Momma et al., 2002). This problem can only be better resolved long after the earthquakes by exclusive submersible exploration, bathymetric surveys, or drilling in a hindcasting prospective (Tappin et al., 2014). Thus, whether to adopt an open (nonzero slip) or closed (zero slip) boundary along the upper fault edge is a difficult decision, leaving a substantial range of tsunami estimations. The primary objective of this study is to study such ranges of tsunami predictions by performing inverse analyses of GPS displacements induced from hypothetical Cascadia events. We test the hypothesis that the different boundary conditions of the inverse analysis contribute to significantly different estimates of seafloor displacement and tsunami forecasts along the coast.

2. Tsunami Hazard of Cascadia

Severe seismic and tsunami hazards are known within the Cascadia Subduction Zone (CSZ) based on multidisciplinary records (Clague, 1997; Geist, 2005; Rogers & Dragert, 2003). Episodes of aseismic creep and seismic tremor events have been observed in the upper plate of the CSZ over the last few decades (Bartlow et al., 2011; Miller et al., 2002; Rogers & Dragert, 2003), while a shallow portion (depth $<$ ~25 km) of the fault is regarded as a "full-rupture" zone and is currently locked (Wang et al., 2003; Witter et al., 2013). Paleoseismological studies reveal that the Pacific Northwest region experienced several megathrust earthquakes and tsunamis in the past 3,500–7,000 years with irregular time intervals averaging ~500 years (Atwater, 1987; Clague, 1997). Since the last *M*9 event in 1700, the hazards arising from any upcoming megathrust earthquakes in the next 200–300 years are importable, prompting a comprehensive study of the seismic and tsunami impact to the coastal areas necessary for urban planning, emergency and resilience strategy purposes (Geist, 2005). Noting that a relatively short distance (~150 km) exists between the trench and shoreline of the Pacific Northwest, destructive tsunami waves can arrive at coastal cities (Table S1 in the supporting information) of northern California, Oregon, Washington, and British Columbia in less than 30 min after a tsunamigenic CSZ event (Wang & Liu, 2006). To improve the early warning of local tsunami

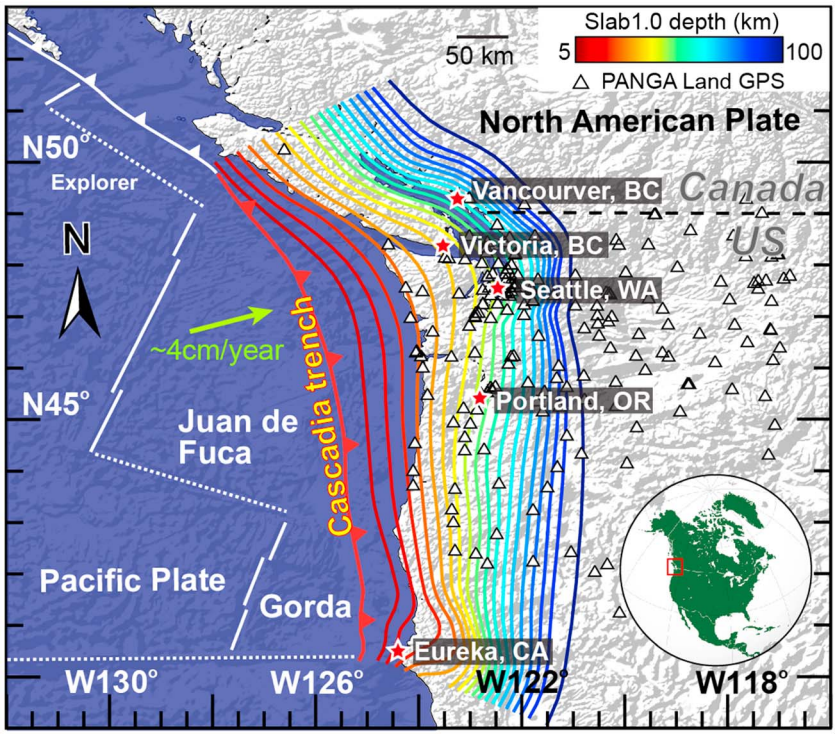

Figure 1. Tectonic settings and Pacific Northwest Geodetic Array (PANGA) Global Positioning System (GPS) network in Pacific Northwest. Cascadia Subduction Zone resides between North American Plate and Pacific Plate plus several microplates such as Explorer, Juan de Fuca, and Gorda Plate, converging at ~4 cm/year (Dragert et al., 2001). The colored contours denote slab geometry constrained by Slab1.0 (Hayes et al., 2012), below multiple populated cities (red stars). Onshore real-time GPS stations of the PANGA network are shown as triangles. The bottom right inlet shows the map location.

impacts, the recent upgrade of real-time submarine and onshore GPS networks (e.g., Pacific Northwest Geodetic Array [PANGA], University NAVSTAR Consortium Plate Boundary Observatory, and U.S. Geological Survey networks) in the Cascadia region have new windows for monitoring continuous ground movements and delivering instantaneous crustal response upon significant seismic events (Austin et al., 2013) (Figure 1). Here our study focuses on a PANGA-GPS-based inverse analysis of two hypothetical *M*9 earthquake scenarios to test our hypotheses concerning the domain heterogeneity and rupture boundary conditions.

3. Methods

The objective of this study is to investigate how different approximations of the crustal domain and near-trench rupture boundary conditions affect the solutions of tsunami sources resolved by GPS-based inverse analyses, and thereby modify the predictions of tsunami wave amplitude. Case studies for the CSZ are carried out to estimate tsunami hazard using rich geodetic data availability along the Pacific Northwest. The numerical implementation is divided into two parts, namely, seismic deformation modeling and tsunami modeling. The former involves both forward and inverse analyses of synthetic GPS data, while the latter only computes tsunami propagation in a forward manner. The details of the methodology are described in the following sections.

3.1. Real-Time GPS Network and Inverse Analysis

To test the hypotheses regarding the sensitivity of resolved seafloor deformation and tsunami forecast to the solutions of inverse analyses, synthetic ground displacements are calculated at 203 real-time GPS stations of the PANGA, which are deployed intensively along the coast and further penetrate ~500 km inland along the CSZ (Miller et al., 2002) (Figure 1 and Table S2). Among several existing high-rate GPS networks, PANGA is chosen because of its good station density and distribution, as well as the data accessibility. Both raw and processed data are readily available online (http://www.geodesy.cwu.edu/data) in a near real-time manner,

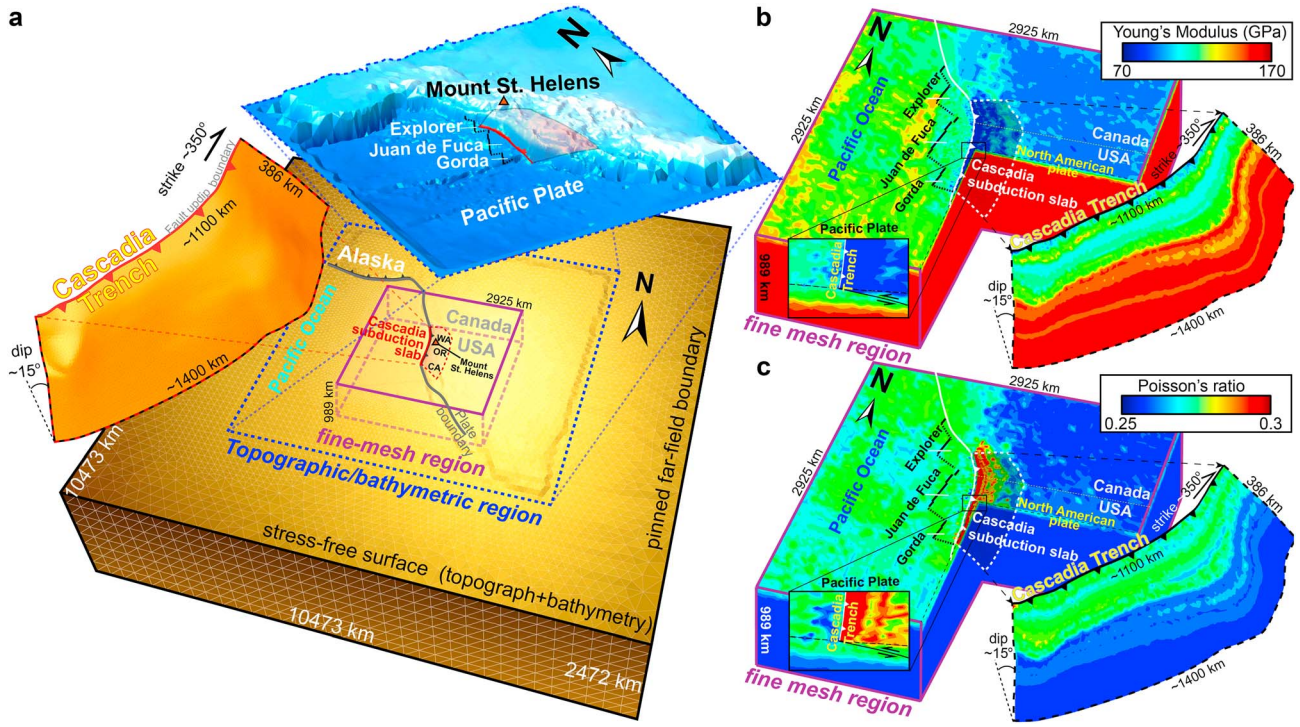

Figure 2. Finite element deformation model. (a) Finite element model domain assembles lithospheric and tectonic environment of North America and Western Pacific Ocean, spanning (from the north) over the West Coast of U.S., Canada, and Mexico. The square domain block is of dimension, 10,473 × 10,473 × 2,472 km^3 (width × length × depth), carrying ~20,000 nodes and ~1 million first-order tetrahedral elements. A fine-mesh region (FMR) (purple box) is near Pacific Northwest region for a refined model resolution near the trench (red line). Cascadia subduction slab (left) is embedded in FMR with a mesh size of 10 km (on-slab). The domain top is a stress-free surface shaped by irregular topography and bathymetry based on ETOPO1 (Amante & Eakins, 2009). The topographic/bathymetric region (blue area) is zoomed in to show near-field elevation and tectonic structures in a 3-D manner (top). Heterogeneous crustal material is defined by 3-D distribution of (b) Young's Modulus and (c) Poisson's ratio based on CRUST 2.0 (Bassin et al., 2000). Weaker upper layer (0–130 km) is characterized by small values of Young's modulus (<120 GPa), whereas crustal layer beneath 150 km is significantly stronger with Young's modulus being as high as 170 GPa. Material heterogeneity/contrast across subduction margin is well reflected by distinctive changes of elastic moduli from oceanic domain to continental domain.

providing the research community a unique opportunity to monitor the crustal deformation and model tsunami genesis (Wei et al., 2014). Compared with the Tohoku, Japan region, the proximity of the trench to the nearest land-based GPS stations in the CSZ warrants better creditability of tsunami source characterization through GPS data (cf. Masterlark, 2003; Wei et al., 2014) (Figure 1). For simplicity, we do not include any oceanic observations in this study.

To investigate a seismic source, we solve the linear inverse problem to estimate (calibrate) the dislocation vector, **m**, of a fault slip distribution from the observed surface displacement (GPS-based), **d** (calibration targets), (Aster et al., 2011; Masterlark, 2003; Menke, 2012) by

$$\begin{bmatrix} G \\ \beta L \end{bmatrix} m = \begin{bmatrix} d \\ 0 \end{bmatrix} \tag{1}$$

where **G** is the matrix of Green's functions, β is the regularization coefficient, and **L** is the Laplacian smoothing matrix equivalent to the FEM-approximated global conductance matrix (GCM) across the fault curvature (Hughes et al., 2010). Open ($\nabla^2\mathbf{m} = 0$) and closed ($\mathbf{m} = 0$) boundary conditions are applied along the top edge of fault and inherited in GCM_{open} and GCM_{closed}, respectively, to designate a surface-breaking or nonsurface-breaking rupture. The remaining three edges have zero slip conditions. This configuration is crucial for accurately resolving dislocation/tsunami sources (whether it is a tsunami earthquake) and is one of the main foci of our study. **G** characterizes the fault slip behavior of each subfault patch (Figure 2) along a structural discontinuity with respect to a particular suite of geodetic observations (Figure 1). Each element entry, $\mathbf{G}_{ij}$ represents the contribution to the displacement of d_j due to unit dislocation of subfault node pair m_i. Here d_j refers to the synthetic displacement of each selected PANGA station, while $\mathbf{G}_{ij}$ is computed in either a uniform or nonuniform domain to explore the impact of crustal material complexities (Figure 2).

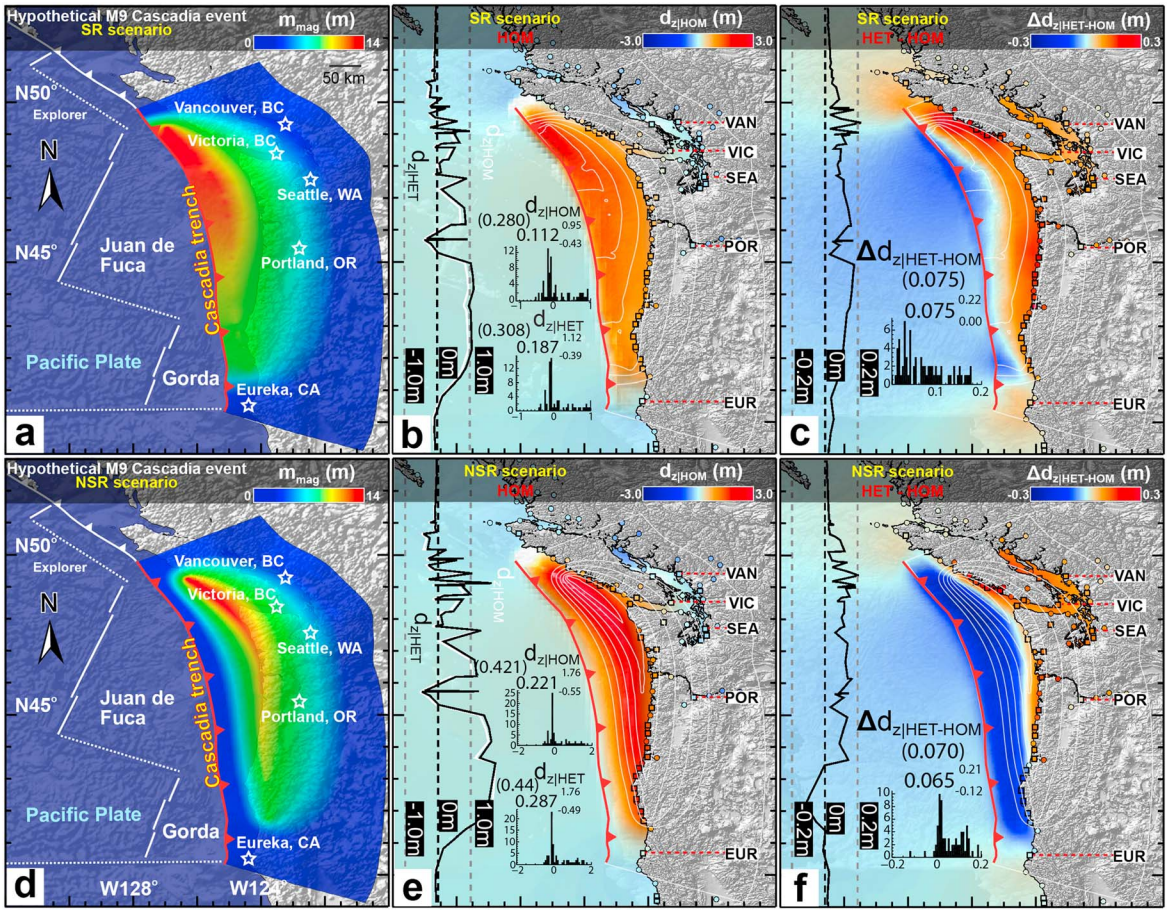

Figure 3. Comparison of forward-modeled seafloor deformation between heterogeneous (HET) and homogeneous (HOM) for surface-rupturing (SR) and nonsurface-rupturing (NSR) scenarios. Hypothetical earthquake scenarios of (a) SR and (e) NSR are studied. Most slips are concentrated above 30 km with negligible slips shown in blue. For SR case, (b) predicted seafloor deformation in HOM, $d_{z|HOM}$ subtracts that in HET, $d_{z|HET}$, revealing (c) model difference ($\Delta d_{z|HET-HOM} = d_{z|HET} - d_{z|HOM}$). Similarly, (e) predicted seafloor deformation of NSR scenario in HOM, $d_{z|HOM}$ subtracts that in HET, $d_{z|HET}$, showing (f) model difference. Coastal runup checkpoints and major cities are denoted by circles and squares, respectively. The linear profiles (left) of each subfigure refer to values at coastal checkpoints, while the white contours represent the slip. The bracket, digit, subscript, and superscript designate mean of absolute value, mean, minimum, and maximum as indicated by corresponding frequency-distribution bar charts.

3.2. Hypothetical Scenarios

The trench margin of the CSZ curves inland and dips to the east with the strike direction changing from north to northwest with latitude, generally in alignment with the coastline of Pacific Northwest (Figure 1). We select two pseudo megathrust scenarios along the CSZ (Figures 3a and 3d) to study the sensitivity of tsunami predictions to seafloor deformation (Table S3). The majority of fault slip is generally concentrated above the depth of ~30 km, overlapping with the full-rupture seismic zone (Schmalzle et al., 2014), and tapering off in the transition zone (Oleskevich et al., 1999; Priest et al., 2010) and the zone of episodic tremor and slip (Gao & Wang, 2017). These two scenarios are trench-rupturing (zero slip along the trench, Figure 3a) and nontrench-rupturing (nonzero slip gradient along the trench, Figure 3d), respectively, with pure reverse faulting. Contrasting coastal subsidence/uplift predications are expected for these two scenarios (Grilli et al., 2013). For simplicity, we do not consider the splay-fault geometry which is aligned with the trench location specifically near the southern CSZ (Witter et al., 2013). Most synthetic slips are located in the west and southwest of Vancouver Island (Figure 3) which has accumulated a considerable amount of slip deficit (McCaffrey et al., 2007, 2013; Schmalzle et al., 2014). The projected rupture peaks (max. ~14 m) occur near the northern CSZ and gradually taper southward near Washington, and eventually fade out near Northern California (Figures 3a and 3d). Both seismic scenarios are equivalent to a moment magnitude of ~9, with average slip of 4.3–4.8 m over the curved slab surface of area ~5×10^5 km^2 (Hayes et al., 2012). The megathrust slip distributions follow a Laplacian spatial relation (cf. Hughes et al., 2010; Masterlark, 2003).

3.3. Finite Element Models

Our FEMs of elastic dislocation are designed to assemble the complex tectonic environment of the CSZ and the surrounding region of North America (Figure 2), which is a significant difference from the existing half-space (Okada, 1985) and layered models (Eleonora et al., 2002; He et al., 2003; Savage, 1998; Xu et al., 2010). Throughout the studies, FEMs are responsible for computing deformation from different earthquake scenarios either within a heterogeneous (HET) or HOM crustal domain in a quasi-static regime. The FEMs are constructed with the commercially available finite element code, *Abaqus* (www.3ds.com/products-services/simulia/products/abaqus), which is capable of accommodating a variable distribution of anisotropic material properties and fault curvature. The governing equations for a three-dimensional elastic domain of spatially variable material properties are

$$\frac{\partial}{\partial x_j}\left[G(x)\left(\frac{\partial u_i}{\partial x_j}+\frac{\partial u_j}{\partial x_i}\right)\right]+\frac{\partial}{\partial x_i}\left[\lambda(x)\left(\frac{\partial u_k}{\partial x_k}\right)\right]\delta_{ij}=f_i \& \delta_{ij}=\begin{cases}0, i\neq j\\ 1, i=j\end{cases} \tag{2}$$

where x_i is a spatial component of coordinate axes $\mathbf{x_i}$, and u is the corresponding displacement; G is the shear modulus, and λ is the Lame's parameter; f_i denotes a source term or a body force; subscripts i and j represent the orthogonal coordinates of the x, y, and z axes. Subscript k refers to the summation over i and j with δ_{ij} being the delta function. The realistic slab geometry of the CSZ is configured according to the tomography- and seismicity-based Slab1.0 subduction model (Hayes et al., 2012) (https://earthquake.usgs.gov/data/slab/models.php), inheriting variable strike and dip among subfault patches (Figures 1 and 2 and Table S3). The megathrust curvature attains a mean width of ~400 km and length of ~1,300 km, overall striking northward at ~350° and dipping to the east at ~15° (Figure 2a). The strike of the trench curvature changes considerably near Vancouver Island and Seattle and makes the slab gently convex inland (Figures 1 and 2).

The square FEM domain is centered at [45°N, 125°W] with ~10,500 km in width/length and ~2,500 km in thickness (Figure 2 and Table S4). The fault entity is converted into a shell object (.sat) through a python-driven 3-D graphic code, Rhino3d (www.rhino3d.com), which creates a 3-D entity of subfault locations to preserve the realistic subduction settings of Cascadia. This shell object is then imported into *Abaqus* to shape the 3-D fault geometry in an FEM domain. From the CRUST2.0 velocity repository (http://igppweb.ucsd.edu/~gabi/crust2.html), the distributed rock properties are specified by spatially variable Young's modulus, E (Figure 2b), and Poisson's ratio, v (Figure 2c), which are formulated by

$$\boldsymbol{E}=\frac{\rho V_s^2\left(3V_p^2-4V_s^2\right)}{V_p^2-V_s^2} \& \boldsymbol{v}=\frac{V_p^2-2V_s^2}{2\left(V_p^2-V_s^2\right)} \tag{3}$$

where V_p, V_s, and ρ represent the p wave velocity, s wave velocity, and density, respectively.

The domain tessellation comprises ~200,000 nodes and ~1,000,000 first tetrahedral elements and is meshed nonstructurally through the Abaqus-CAE module. The fault discontinuity is encapsulated in a fine-mesh region (width/length = ~3,000 km and depth = ~1,000 km) for a refined near-field resolution (Figures 2a and 2b). The element dimension is ~10 km over the fault surface and scaled up to 40 and 150 km along the fine-mesh region rims and the far-field boundaries, respectively. A total of 5,447 subfault node pairs are stitched together to simulate the HET slip distribution over the curved fault surface. Given equilibrium initial conditions, the elastic dislocation is formulated by the kinematic constraint equations over these subfault node pairs (Masterlark, 2003). The far-field lateral and depth boundary of the domain are pinned and constrained by the outer block surfaces. The FEM top is a stress-free surface representing the Earth's surface. This surface is shaped by the land topography and seafloor bathymetry according to ETOPO1. Through sequentially slipping each of subfault node pair separately by a unit dip-slip and strike-slip, the composite Green's function matrix, $\mathbf{G}_i$ of each individual subpatch is generated and aggregated to prepare for the linear inverse analyses. We perform series of 2-D linear interpolation to extract the whole Green's function matrix, $\mathbf{G}$ for the targeting GPS stations, and $\mathbf{d}$ from the simulated displacements of FEM surface nodes (Figure 2). This linear interpolation precisely corresponds to the first-order finite element formulation.

The above FEM configurations (Table S4) have been verified against the customary half-space analytical solutions (e.g., Okada, 1985) in an HOM domain of Westerly granite (Wang, 2000) (Figure 4 and Table S5). The Cascadia subduction slab is first approximated by a rectangular discontinuity (width~372 km and

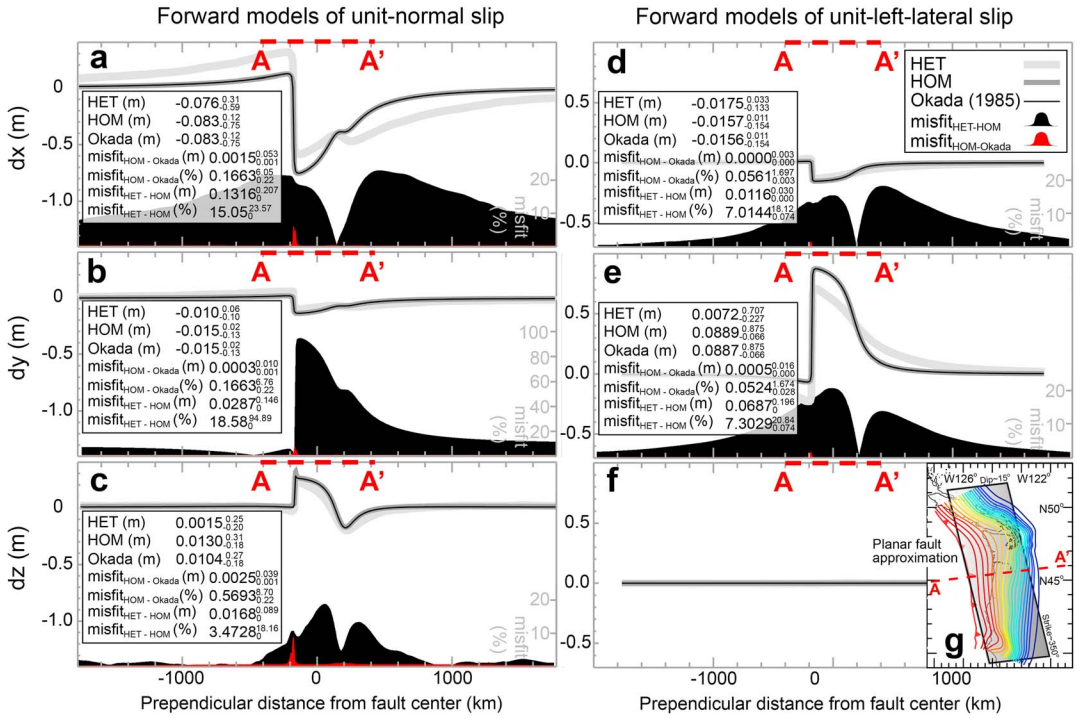

Figure 4. Finite element model validation against Okada half-space solution. Three-dimensional deformation predictions (d_x, d_y, d_z) of (a–c) unit-normal and (d–f) unit-sinistral slips in homogeneous (HOM; dark gray line) are plotted along an along-dip profile AA′ of an approximated planar dislocation (right bottom inlet), showing a consistency of up to 99.5% with Okada half-space solution (black line) (Okada, 1985). Predictions of heterogeneous (HET; light gray line) are also compared with those of HOM and Okada models to highlight influence of spatially varying elastic materials. For each component, the bottom shaded plots reveal model misfits for HET versus HOM (black) and HOM versus Okada (red). In each box, the value, subscript, and superscript refer to the mean, minimum, and maximum of model-prediction misfit. Configuration of a HET crust causes significantly different signatures of surface deformation (misfit up to 19%) from a HOM domain.

length~1,364 km) sharing similar strike (~350°) and dip (~15°) characteristics (Figure 4g). The analytical Okada solutions of uniform unit-thrust (Figures 4a–4c) and unit-sinistral (Figures 4d, 3e, and 3f) slips are compared with the numerical FEM solutions within a 3-D deformation field (d_x, d_y, and d_z) to validate the FEM configurations. Robust compatibility of up to 99.5% is confirmed between the analytical and HOM solutions, with negligible misfits (<0.0025 m) for all three displacement components (Figure 4 and Table S5). On the contrary, the model misfits climb to 0.17 m (~19%) when comparing the results between HET and HOM, especially for the unit-thrust dislocation (Figure 4b). These preliminary results have already implied the potential discrepancy of modeling seafloor deformation between HET and HOM, which might influence the tsunami analysis and requires further studies. Elastic element formulations are verified and benchmarked by Abaqus, Dassault Systèmes Simulia Corp. (Abaqus Verification Manual and Benchmarks Manual, http://abaqus.software.polimi.it/v6.12/index.html). We assume that the HOM validation also applied to the HET models because they share the same mesh and domain boundary condition configurations.

3.4. Tsunami Modeling

After a seismic-slip distribution is derived, the numerical modeling of tsunami involves two steps: (1) simulations of seafloor deformation and (2) wave propagation. For the purpose of our study, we assume an instantaneous initial condition for the tsunami genesis adopted by existing studies (Fujii et al., 2011; Goda et al., 2014; González et al., 2009; Newman et al., 2011; Ulutas, 2013; Uslu et al., 2007), neglecting the sensitivity to rupture velocity and horizontal movements (cf. Fujii & Satake, 2007) and presuming an instantaneous transfer of the vertical disturbance from the seafloor to the ocean surface (Kajiura, 1970). To test the hypothesis of domain heterogeneity, the initial seafloor deformation is calculated from the FEM-based seismic deformation field in both HET and HOM (Figure 2), instead of using customary Okada half-space solutions. The seismically triggered seafloor displacements are interpolated to a nested grid of a fluid domain covering the coastline of Pacific Northwest. The wave propagation is governed by nonlinear shallow-water (or

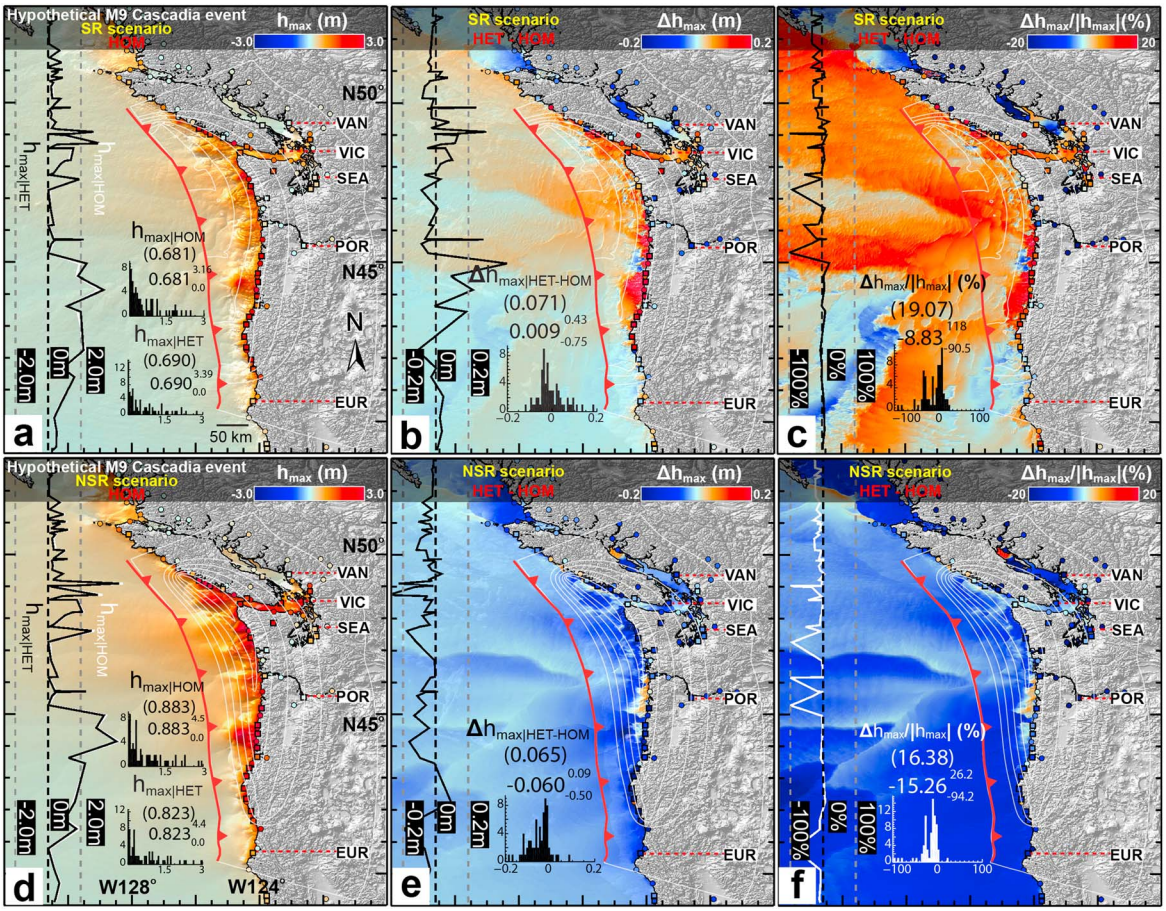

Figure 5. Comparison of forward-modeled maximum tsunami height between heterogeneous (HET) and homogeneous (HOM) for surface-rupturing (SR) and nonsurface-rupturing (NSR) scenarios. For SR case, (a) predicted maximum tsunami height in HOM, $h_{max|HOM}$ subtracts that in HET, $h_{max|HET}$, revealing (b) model difference ($\Delta h_{max|HET-HOM} = h_{max|HET} - h_{max|HOM}$) and (c) percentage difference ($\Delta h_{max|HET-HOM}/|h_{max|HOM}|$). Similarly, (d) predicted maximum tsunami height of NSR scenario in HOM subtracts that in HET showing (e) model difference and (f) percentage difference. Linear profiles (left) of each subfigure refer to values at coastal checkpoints.

longwave) equations within a moving boundary and explicit Leap-Frog scheme of a finite difference method (Wang, 2008; Wang & Power, 2011). The tsunami simulation is implemented through a Fortran-based software package, Cornell Multi-grid Coupled Tsunami model developed by Wang and Liu (2006). We consider only seafloor deformation (i.e., no submarine mass failures) for generating tsunami waves. Different resolutions of topography/bathymetry are configured in two telescoped grids with increasing spatial resolutions for efficiently calculating tsunami waveforms and coastal tsunami heights. The larger regional grid of West Pacific (0°–60°N, 170°–100°W) is resampled from the ETOPO1 with a grid interval of 10 arcmin, whereas an encapsulated local grid of the CSZ (39°–53°N, 132°–119°W) maintains a finer 2 arcmin resolution for more prediction details of near-field tsunami impact (Figure 3). Open-ocean boundary conditions were applied along the perimeter of the coarser grid. A time step of 1 s is used to satisfy the stability condition of finite difference method for both far- and near-field computations. The tsunami propagation during the first 5 hr after the earthquake is simulated to forecast the maximum coastal amplitude, at a computational speed of 14 min/hr. The time series of wave profile are saved at every 300 s of the postseismic period for further analyses. The above simulation is performed on a workstation with a 16-node CPU of 3.0 GHz and RAM of 64 GB.

4. Results

The tsunami modeling is conducted with a surface-rupturing (SR) (Figure 3a) and nonsurface-rupturing (NSR) (Figure 3d) *M*9 scenario along the CSZ. We present the results of the sensitivity analysis in the framework of forward (Figures 3–7 and S1 and S2 in the supporting information) and inverse problems (Figures 8–15 and

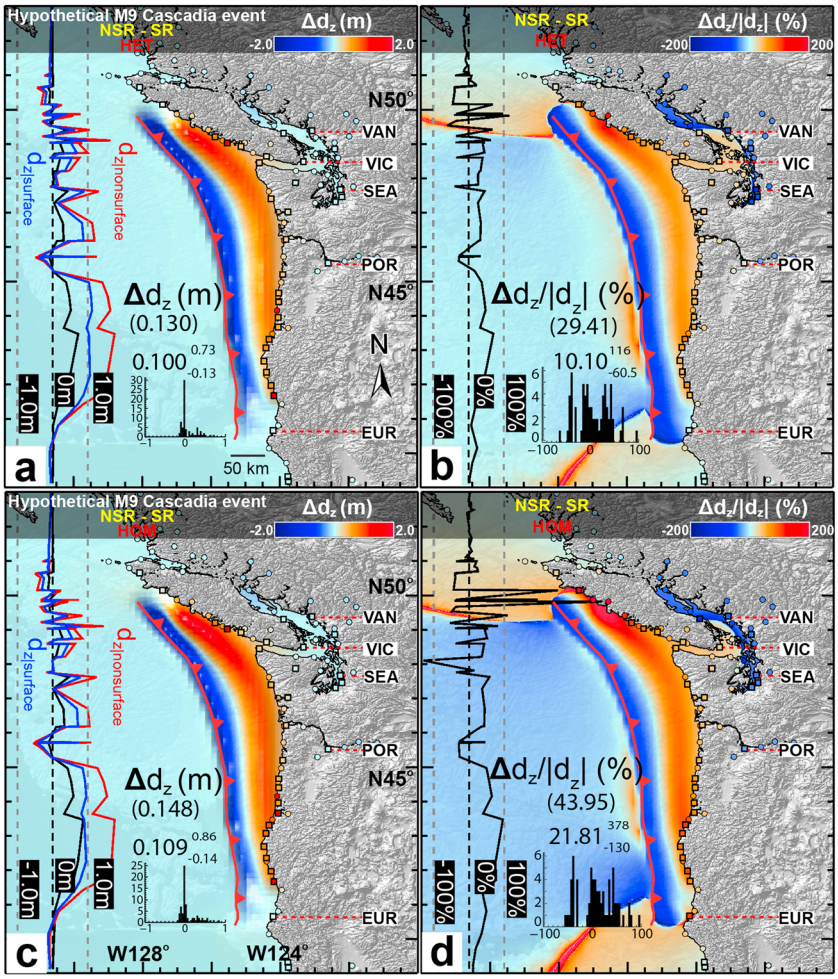

Figure 6. Comparison of forward-modeled seafloor deformation between surface-rupturing (SR) and nonsurface-rupturing (NSR) scenarios. Predicted seafloor deformation by NSR scenario, $d_{z|NSR}$ (Figure 3e), is subtracted by that of SR scenario, $d_{z|SR}$ simulated in homogeneous (HOM; Figure 3b) and heterogeneous (HET). This yields prediction difference, $\Delta d_{z|NSR\text{-}SR} = d_{z|NSR} - d_{z|SR}$, in (a) HET and (c) HOM, and percentage difference ($\Delta d_{z|NSR\text{-}SR}/|d_{z|SR}|$) in (b) HET and (d) HOM. Linear profiles (left) of each subfigure refer to values at coastal checkpoints.

S4–S8). The initial seafloor deformation is simulated in both HET and HOM for testing the model dependency on different crustal domains. In particular for the inverse analyses, different boundary conditions are incorporated for examining possible artifacts of misinterpreting near-trench-rupturing behavior on simulating tsunami wave dynamics. The near-field tsunami forecasts from deformational models are investigated and compared through three descriptive quantities, namely, initial seafloor deformation, d_z; maximum tsunami wave height, h_{max}; and the arrival of maximum tsunami wave height, t_{hmax}.

4.1. Forward Analysis of Seafloor Deformation and Tsunami

Forward models of fault elastic dislocation calculate the quasi-static deformation due to the sudden fault rupture buried beneath the surface (Masterlark, 2003; Okada, 1985). Through considering both the SR and NSR scenarios, we study how underground crustal material and slip distribution result in different initial seafloor/surface conditions for tsunami genesis.

4.1.1. Heterogeneous Versus Homogeneous Domain

4.1.1.1. Surface-Rupturing Scenario

In HOM, the SR scenario of magnitude ~9.2 gives rise to the peak vertical deformation, d_z, of ~3 m near the west coast of Vancouver Island (Figures 3a and 3b). The seafloor deformation displays an oval-shaped pattern (~100 × 400 km) along the curved trench and tapers gradually southward, in accord with the underlain slip asperity diminished at ~45°N (Figure 3b). The coastline generally experiences an average

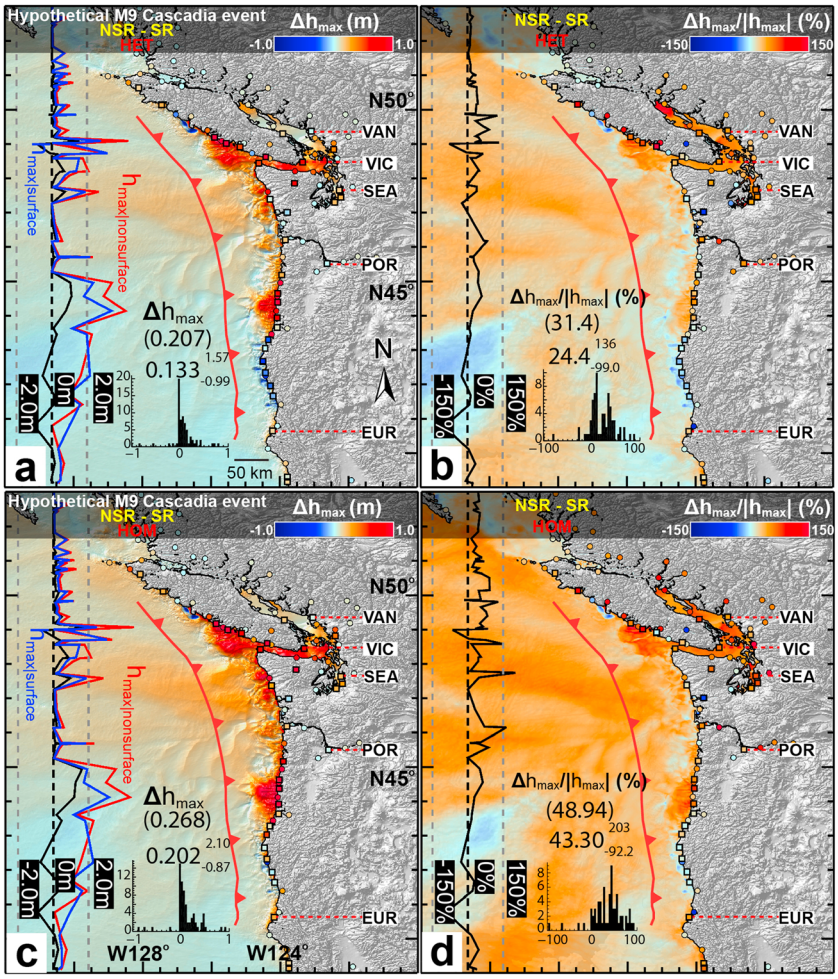

Figure 7. Comparison of forward-modeled maximum tsunami height between surface-rupturing (SR) and nonsurface-rupturing (NSR) scenarios. Predicted maximum tsunami height by NSR scenario, $h_{max|NSR}$ (Figure 4d) is subtracted by that of SR scenario, $h_{max|NSR}$ simulated in homogeneous (HOM; Figure 4a) and heterogeneous (HET). This yields prediction difference, $\Delta h_{max|NSR\text{-}SR} = h_{max|NSR} - h_{max|SR}$, in (a) HET and (c) HOM, and percentage difference ($\Delta h_{max|NSR\text{-}SR}/|h_{max|SR}|$) in (b) HET and (d) HOM. Linear profiles (left) of each subfigure refer to values at coastal checkpoints. Linear profiles (left) of each subfigure refer to values at coastal checkpoints.

uplift of 0.1–0.2 m which transforms into inland subsidence (max. 0.4 m) along the Columbia River near Portland and the channel directing to the Vancouver-Seattle (VAN-SEA) area. The coastal cities typically experience the maximum tsunami height, h_{max} ~0.7 m (Figure 5a) with the highest height (~3.4 m) near Western Oregon (~45°N) and Southwestern Vancouver Island (~49°N). The VAN-SEA area has relatively smaller h_{max} less than 0.5 m as the hydraulic energy is dispersed in the inner bay/fan area between 47°N and 50°N (Figure 5a).

In HET, we observe a contrasting deformation pattern to HOM. The weaker continental crust (high Poisson's ratio ~0.36 in Figure 2) amplifies the offshore uplift by up to 0.3 m principally near the west coast of Vancouver Island and Oregon (Figure 3c). In these areas, such nonuniform material distribution of HET roughly contributes to an additional ~20% of seafloor displacements (Figures 3b and 3c), which cannot be recovered by HOM. This underestimation of displacements by HOM propagates into the tsunami model, as reflected by the waveform (Figure 5) and the arrival time (Figure S1). The predicted tsunami heights are altered near the shore and shown with an extra height averaged at ~0.1 m (Figures 5b and 5c). Some coastal localities receive larger h_{max} (by max. ~0.4 m) particularly near the west of Vancouver Island and Oregon, while smaller h_{max} are observed sparsely along the west coast of Washington State and the estuary of Columbia river, reflecting an average uncertainty of ~20% in the HOM-based tsunami predictions (Figures 5b and 5c).

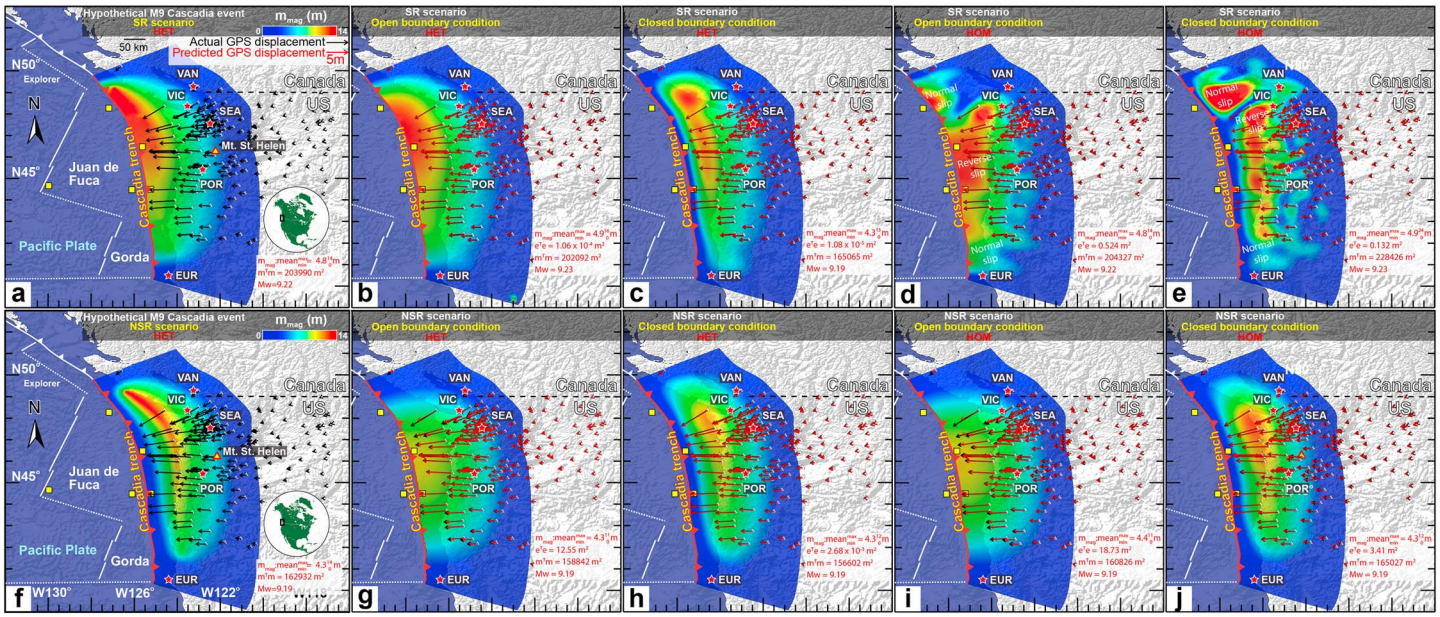

Figure 8. Global Positioning System (GPS)-based inverse analysis of synthetic slip distributions within heterogeneous (HET) and homogeneous (HOM) using different rupture boundary conditions. *M*9 earthquake scenarios of (a) surface-rupturing (SR) and (f) nonsurface-rupturing generate synthetic GPS movements in HET to mimic realistic coseismic surface deformation. Most slips are concentrated above 30 km with negligible slips shown in blue. These pseudo geodetic signals (black arrows) are then inverted with $G_{HET/HOM}$ and $GCM_{open/closed}$. For each scenario, tsunami is triggered by seafloor displacements resolved through four different inversion schemes, namely, (b and g) HET_OPEN, (c and h) HET_CLOSED, (d and i) HOM_OPEN, and (e and j) HET_CLOSED. Predicted GPS displacements are plotted as red arrows, overlaying derived fault slip distribution from each scheme. For SR scenario, slips are best recovered by (b) HET_OPEN, which reproduces a consistent SR pattern. Slip distribution is poorly recovered in HOM (d and e) exhibiting nonrealistic artifacts of normal slips, especially near the south of Vancouver Island and Northern California. Similarly for the NSR scenario, slips are also best recovered in HET with null-trench-slipping boundary condition, by (h) HET_CLOSED, which reproduces similar subsurface rupturing and gives the smallest error misfit of 2.68×10^{-3} m^2 among other schemes (g, i, and j). Failure of adopting closed rupture boundary conditions propagates slips near trench (g and i), resulting in underestimated GPS movements near the coast in comparison with the results of compatible trench-rupture boundary conditions (h and j). In general, prediction errors of both scenarios are significantly larger when using G_{HOM} (d, e, i, and j) over G_{HET} (b, c, g, and h), regardless of rupture boundary conditions.

4.1.1.2. Nonsurface-Rupturing Scenario

In HOM, the NSR scenario results in wide-spread uplift parallel to the coastline (Figures 3d and 4e). The peak seafloor deformation (d_z ~3.2 m) displays a sausage-shaped pattern (~100 × 800 km) along the continental shelf (43°N–50°N) and gradually tapers inland, corroborating with the underlying fault slip distribution (Figure 3e). The shore is generally uplifted by ~0.2–0.3 m, which is ~50% more than that of the SR scenario (Figure 3b). The west-coast cities of Vancouver Island and Oregon (e.g., Newport and Florence) receive up to 4.5 m of tsunami wave (Figure 5d). The average magnitude of h_{max} along the coast is ~0.82 m which is ~20% larger than the SR scenario (~0.69 m).

In HET, the deformation pattern is again different from that of HOM (Figures 3e and 3f). The weaker upper crust increases the seafloor uplift by up to ~0.2 m over a narrow alongshore region ~20 km away from the coast but substantially reduce seafloor uplift (max. 0.3 m) near the trench (Figure 3f). This contributes to an additional ~20% of seafloor uplift near the coastal cities (Figures 3e and 3f), which cannot be recovered by HOM. Consequently, the predicted $|h_{max}|$ by HET are averagely 0.1 m (~15%) smaller than those by HOM with relatively large discrepancy (~0.2 m) near Vancouver Island (~49°N), Aberdeen (~47°N), and Florence (~44°N) in addition to minor local fluctuations (Figures 5e and 5f).

4.1.2. Surface-Rupturing Versus Nonsurface-Rupturing Scenario

Apart from studying the model prediction differences between HET and HOM, we directly compare the two scenarios of SR (Figure 3a) and NSR (Figure 3d) tsunami sources (Figures 6 and 7). As the NSR source is closer to the coast than the SR source, the NSR scenario has the maximum wave arriving ~10 min earlier than the SR scenario (Figures S2a and S2c) consistent with what is suggested by Satake et al. (2013). More surface uplift (up to 1 m or 30–40%) but less uplift (max. ~2 m) are induced by the NSR scenario near the shore and over top of the trench respectively (Figures 6a and 6c). The SR-NSR discrepancy of nearshore uplift increases

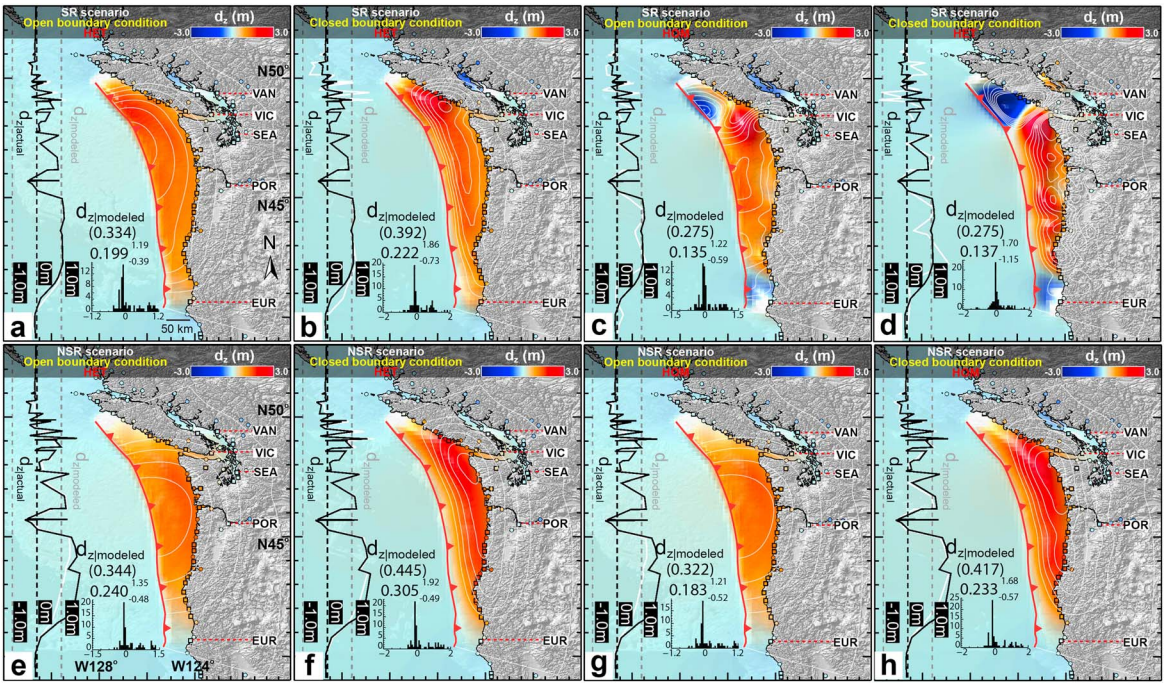

Figure 9. Inversely resolved coseismic seafloor deformation within heterogeneous (HET) and homogeneous (HOM) using different rupture boundary conditions. Inverse solutions of (a–d) surface-rupturing (SR) and (e–h) nonsurface-rupturing (NSR) scenario generate different signatures of coseismic seafloor deformation, d_z. Both (a, b, e, and f) HET- and (c, d, g, and h) HOM-based Green's function matrices are adopted with two types of trench-rupture boundary conditions, namely, (a, c, e, and g) open and (b, d, f, and h) closed. For each scenario, the tsunami is triggered by seafloor movements resolved from four different inversion schemes, namely, (a and e) HET_OPEN, (b and f) HET_CLOSED, (c and g) HOM_OPEN, and (d and h) HOM_CLOSED. Linear profiles (left) of each subfigure refer to modeled (white) and actual (black) deformation respectively at coastal checkpoints which are best evaluated in (a) and (f) for both scenarios, respectively. The white contours refer to the inverted slip distributions. The bracket, digit, subscript, and superscript designate mean of absolute value, mean, minimum, and maximum as indicated by corresponding frequency-distribution bar chart. For SR case, (c and d) HOM produces substantially different deformation pattern (with unrealistic normal slips) from (a and b) HET due to oversimplification of crustal material. For NSR case, different rupture boundary conditions, namely, (e and g) open and (f and h) closed, incur different estimates of seafloor movements.

southward from ~0.3 m near Vancouver Island to ~0.8–1.0 m near Oregon, providing different conditions for modeling wave dynamics (Figures 6a and 6c). As a result, the subsurface rupture overall encourages a larger coastal $|h_{max}|$ by ~0.13–0.20 m on average which is equivalent to ~24–43% of an SR case (Figures 7b and 7d). On the contrary, smaller maximum amplitudes (Δh_{max} ~−1 m) are predicted by NSR scenario than the SR scenario along the coastal cities of Southern Oregon (e.g., Gold Beach) and Northern California (e.g., Eureka) (Figures 7a and 7c).

4.2. Inverse Analysis of Seafloor Deformation and Tsunami

A common way to constrain tsunami sources is through the inverse analyses of onshore/offshore geodetic observations such as GPS (Blewitt et al., 2009; Hoechner et al., 2008; Ohta et al., 2012; Wei et al., 2014) for imaging seismic slip. Within a realistic HET domain of crustal material (Figure 2), we calculate synthetic GPS displacements of the SR and NSR slips as inputs for the inverse analysis (Figures 8a and 8f). These two sets of 3-D deformation vector are then inverted by four combinations of domain-boundary-condition, namely, HET_OPEN ($\mathbf{G}_{HET}$ + GCM_{open}), HET_CLOSED ($\mathbf{G}_{HET}$ + GCM_{closed}), HOM_OPEN ($\mathbf{G}_{HOM}$ + GCM_{open}), and HOM_CLOSED ($\mathbf{G}_{HOM}$ + GCM_{closed}) for physical slip models (Figures 8 and S3 and Table S6) Both open/closed boundary conditions are imparted into the regularization matrix, $GCM_{open/closed}$, while the HET/HOM configurations of the crustal domain are inherited in the Green's function matrices, $\mathbf{G}_{HET/HOM}$ generated by the corresponding FEM (Figure 2). The variability of inverse solutions is then projected onto that of the forward-modeled seafloor deformation that drives the longwave propagation (Figure 9). Comprehensive analyses are carried out to reveal the impacts of different model domains and boundary conditions on recovering slip distributions and thus modeling tsunami impacts (Figures 8–16 and Table S7).

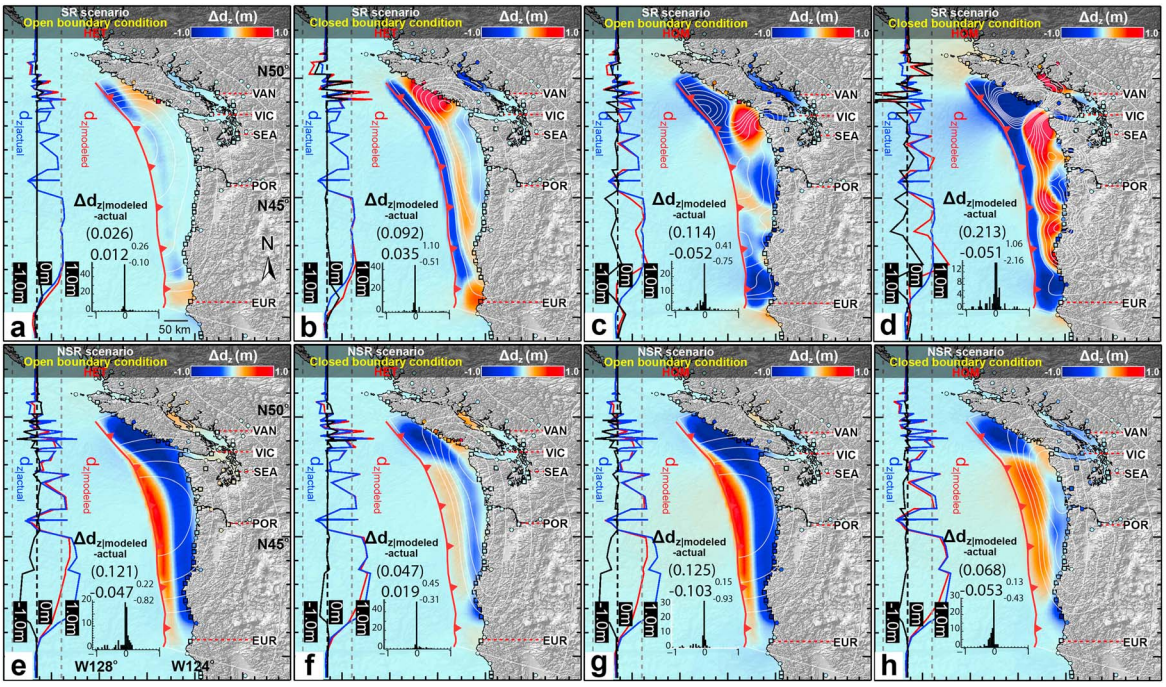

Figure 10. Comparison of modeled and actual seafloor deformation among inverse solutions of different inversion schemes for surface-rupturing (SR) and nonsurface-rupturing (NSR) scenarios. Difference, $\Delta d_{z|\text{modeled-actual}}$ between inverse solutions and actual seafloor deformation is shown for (a–d) SR and (e–h) NSR scenario. For each scenario, tsunami is triggered by seafloor movements resolved from (a and e) HET_OPEN, (b and f) HET_CLOSED, (c and g) HOM_OPEN, and (d and h) HOM_CLOSED. For each inversion scheme, modeled values (red), actual values (blue), and model-actual misfit (black) at coastal checkpoints are plotted in the left of each subfigure. The white contours refer to the inverted slip distributions. Solutions inverted in (c, d, g, and h) homogeneous (HOM) generally attain larger misfits than those in (a, b, e, and f) heterogeneous (HET). Regional model residual is the smallest when SR scenario and NSR scenario are inverted with compatible rupture boundary conditions through (a) HET_OPEN and (f) HET_CLOSED, respectively.

4.2.1. Heterogeneous Versus Homogeneous Domain

4.2.1.1. Surface-Rupturing Scenario

As the buried slab ruptures continuously near the trench, the reverse faulting moves the onshore GPS stations westward. Synthetic GPS displacements show maximum horizontal movements (~8.3 m) among the coastal stations (Figure 8a). The permanent deformation decreases gradually (to ~0.01 m at the easternmost station) when further moving away from the rupturing trench. When inverting the seismic deformation in a HET crustal domain (HET_OPEN), a satisfactory recovery of input slip distribution is obtained, and meanwhile, the surface displacements are nicely predicted with an error misfit, $\mathbf{e}^T\mathbf{e}$, as small as 10^{-4} m^2 (Figure 8b). This slip model is selected from the trade-off curve (*L*-curve) between the misfit and roughness such that the resolved moment magnitude is comparable to the input (Figure S3a). The modeled seafloor deformation is notably consistent (~90%, $\Delta|d_z|$ ~0.03 m) with the actual movements, illustrating exceptionally small deviation ($d_z < 0.01$ m) along the coast of Washington and Oregon (Figures 9a, 10a, and S4a). Such concordance between the input and modeled slip/deformation contributes to an accurate tsunami forecast. The HET_OPEN model well predicts (mean ~94%) the coastal distribution of $|h_{\max}|$ with an accuracy generally better than ~0.03 m (Figures 11a, 12a, and S5a). The model estimate of t_{hmax} (mean ~91 min) (Figure S6a) is readily comparable to the actual arrival (mean~90 min) (Figure S1a).

The recovery of trench-rupturing slip distribution deteriorates when the GPS movements are inverted in a uniform crustal domain (HOM_OPEN) (Figures 8d and S3c). The model misfit jumps more than 3 orders of magnitude from 10^{-4} to 0.5 m^2, in comparison with the abovementioned HET_OPEN predictions (Figure S3a). The corresponding slip solution is different from the input and includes spatially oscillating slips (i.e., alternative nearby reverse and normal slips) (Figure 8d). Spurious normal slips are found near the west coast of Vancouver Island and Northern California, inducing unrealistic seafloor subsidence of 3 m at maximum which does not exist in the input (Figures 9c, 10c, and S4c). Overpredicted and underpredicted seafloor uplift (by up to 1 m) are distributed over the ocean domain between the trench and the coast (Figure 10c). The mean of predicted coastal d_z (~0.14 m in Figure 9c) deviates significantly from the actual values (~0.19 m in

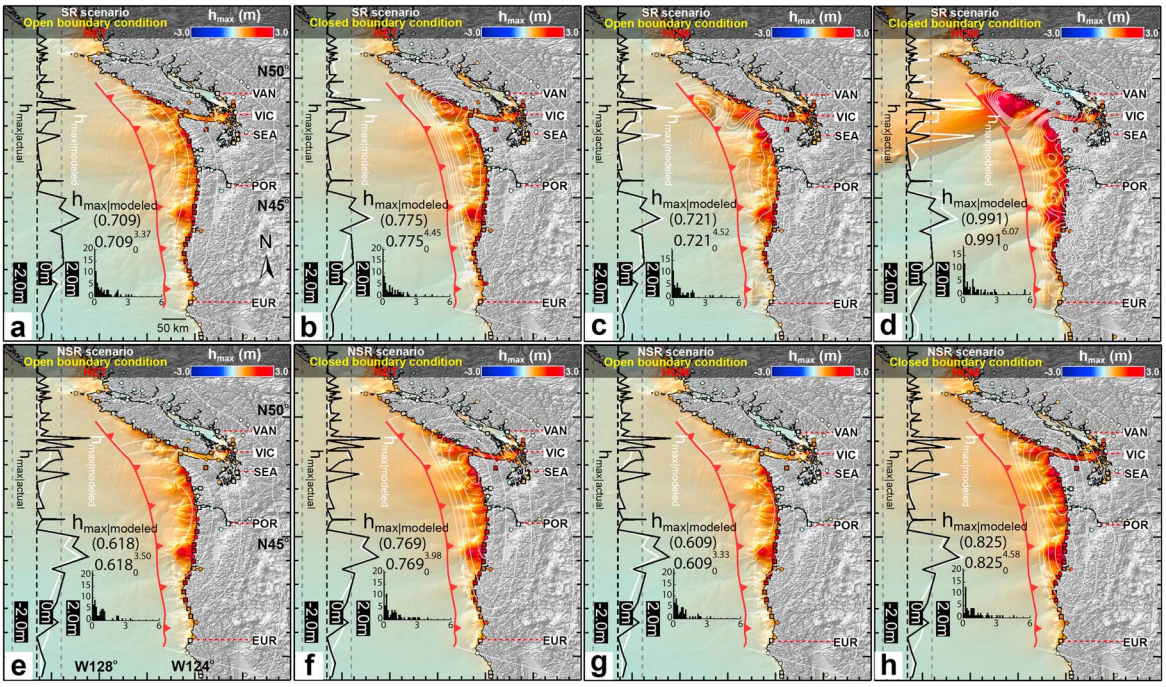

Figure 11. Inversely resolved maximum tsunami height within heterogeneous (HET) and homogeneous (HOM) using different rupture boundary conditions. Inverse solutions of (a–d) surface-rupturing (SR) and (e–h) nonsurface-rupturing (NSR) scenario generate different signatures of maximum tsunami height, h_{max} regionally. Both (a, b, e, and f) G_{HET} and (c, d, g, and h) G_{HOM} are adopted with (a, c, e, and g) GCM_{open} and (b, d, f, and h) GCM_{closed} alternatively. For each scenario, tsunami genesis is based on seafloor movements resolved from (a and e) HET_OPEN, (b and f) HET_CLOSED, (c and g) HOM_OPEN, and (d and h) HOM_CLOSED. For NSR case, different trench-rupture boundary conditions, namely, open (e and g) and closed (f and h), incur severely different predictions of h_{max}.

Figure 3b) by up to 0.75 m (~100%) near the Northern California (Figures 10c and S4c). The nearshore reception of h_{max} is further altered by this miscalculated d_z revealing overestimated and underestimated values (>1.0 m) near VAN-SEA, Olympic Peninsula, and Northern California (Figures 11c, 12c, and S5c). The arrival of h_{max} is largely coherent with the synthetic model (Figure S7c). Furthermore, we also directly compare the solutions of HET_OPEN (Figure 8b) and HOM_OPEN (Figure 8d). The results are consistent with above findings, showing differential coastal movements up to 0.9 m (~100%) (Figures 13a and 13b) and maximum wave height up to 2 m (~100%) (Figures 14a and 14b). These modeling results elucidate how an incompatible elastic model domain can transfer the uncertainties of simulated deformation into tsunami forecasting through geodetic inverse analyses.

4.2.1.2. Nonsurface-Rupturing Scenario

The sensitivity of tsunami models to domain heterogeneity is also observed for the NSR scenario (Figure 8f). The displacement field of the hypothetical subsurface slips is significantly better fitted by the model from HET_CLOSED (Figures 8h and S3f), yielding an extraordinary small misfit (~10^{-3} m^2), which is ~100 times smaller than that (~3.4 m^2) from HOM_CLOSED (Figures 8j and S3h). Although the slip and deformation patterns between these two schemes look similar visually (Figures 8h and 8j), the subtle details of different asperity locations still affect the coastal reception of h_{max} (Figures 11f, 11h, 12f, and 12h), t_{hmax} (Figures S6f, S6h, S7f, and S7h). The coastal vertical displacements are better predicted by HET_CLOSED (mean Δd_z ~0.02 m) (Figures 9f and 10f) than HOM_CLOSED (mean Δd_z ~0.05 m) (Figures 9h and 10h). HET_CLOSED predicts more accurate h_{max} (Figures 11f, 12f, and S5f) than HOM_CLOSED (Figures 11h, 12h, and S5h) over the ocean domain, highlighting the importance of using HET in forecasting tsunamis. The direct comparison between the solutions of HET_CLOSED and HOM_CLOSED also grants support to the above arguments. Differential coastal movements of up to 0.3 m (Figures 13g and 13h) and maximum wave height up to ~0.6 m (Figures 14g and 14h) are predicted between these two solutions (Figures 8h and 8j). We found that the resolved slips (Figure 8h) near the northern CSZ do not corroborate with the input (Figure 8f) even in the case where the adopted elastic domain and boundary conditions are highly compatible with this NSR scenario. This solution ambiguity could be related to the poor resolution due to the absence of PANGA GPS stations over Vancouver Island (Figure 8). As suggested by Masterlark et al. (2001) and Kyriakopoulos et al.

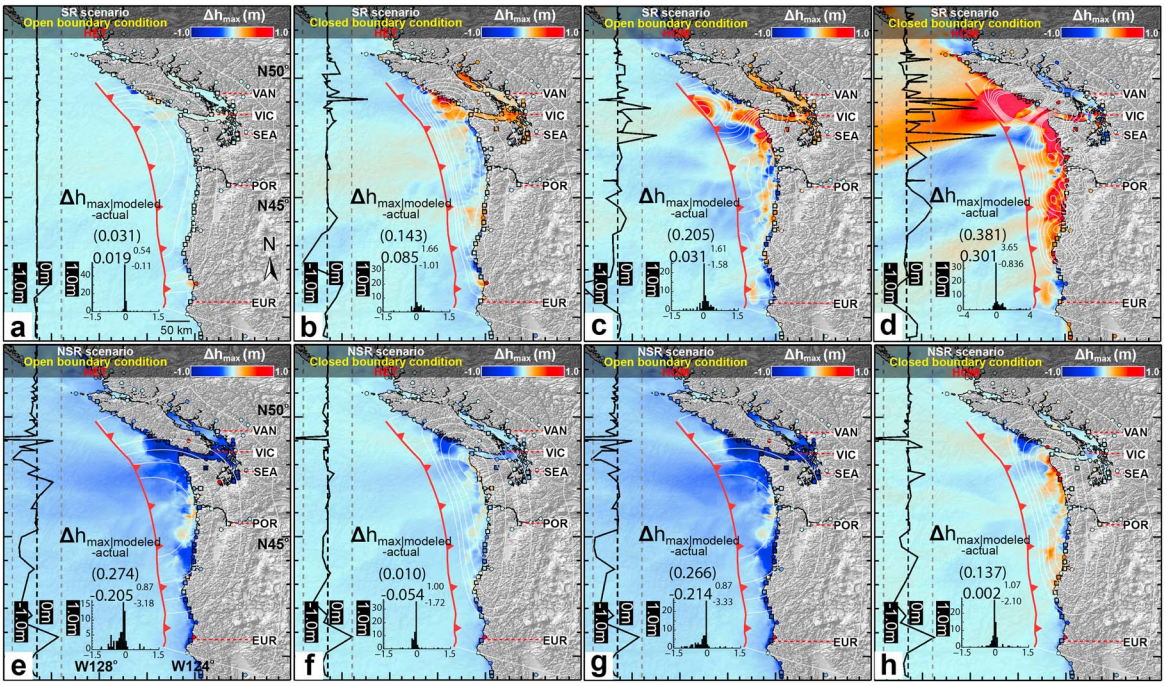

Figure 12. Comparison of modeled and actual maximum tsunami height among inverse solutions of different inversion schemes for surface-rupturing (SR) and non-surface-rupturing (NSR) scenarios. Difference $\Delta h_{\text{max|modeled-actual}}$ between inverse solutions and actual maximum tsunami height is shown for (a–d) SR and (e–h) NSR scenarios. For each scenario, tsunami is triggered by seafloor movements resolved from (a and e) HET_OPEN, (b and f) HET_CLOSED, (c and g) HOM_OPEN, and (d and h) HOM_CLOSED. For each inversion scheme, model-actual misfit (black) at coastal checkpoints is plotted in the left of each subfigure. Solutions inverted in (c, d, g, and h) homogeneous (HOM) generally attain larger misfits than those in (a, b, e, and f) heterogeneous (HET). Regional model residual is the smallest when SR and NSR scenarios are inverted with compatible rupture boundary conditions through (a) HET_OPEN and (f) HET_CLOSED, respectively.

(2013), asperities tend to be resolved near or "pulled" toward those observation points (Figures 8h and 8j), which can be alleviated by including more observation points of other GPS networks (Blewitt et al., 2009).

4.2.2. Open Versus Closed Boundary Conditions

4.2.2.1. Surface-Rupturing Scenario

Apart from comparing slip and tsunami models between HET and HOM, we look into the boundary conditions used for the linear inverse analysis (equation (1)). Given the HET-based Green's function, the synthetic GPS displacements of a surface-breaking rupture are inverted separately with open and closed boundary conditions for imaging the seismic/tsunami source (Figures 8b and 8c). The compatibility between the presumed boundary condition and the actual rupture behavior determines the solution reliability (Menke, 2012). Within expectations, the input slip characteristics of the SR scenario are clearly better recovered by HET_OPEN ($\mathbf{e}^T\mathbf{e}\sim10^{-4}$ m^2) despite HET_CLOSED yielding a slightly smaller misfit ($\mathbf{e}^T\mathbf{e}\sim10^{-5}$ m^2) to the GPS observations (Figures 8b and 8c), revealing how the solutions are dependent to the adopted boundary conditions. This also implies that the goodness of fit to surface displacements is not the only measure to evaluate a slip solution of an underdetermined problem. Though HET_OPEN and HET_CLOSED provide very similar onshore GPS displacements, the predicted offshore deformation differs significantly from each other (Figures 9a, 9b, 10a, 10b, S4a, and S4b). Compared with HET_OPEN, the solution of HET_CLOSED significantly overestimates d_z by up to 1 m (or >100%) near the west coast of Vancouver Island and Northern California (Figures 13c and 13d), with different $h_{\max}$ predictions (Figures 14c and 14d) and an averagely earlier $h_{\max}$ arrival (by ~6 min) (Figure S8b).

4.2.2.2. Nonsurface-Rupturing Scenario

A similar test of different boundary conditions is also conducted with the NSR scenario (Figures 8g and 8h). The near-trench horizontal displacements are significantly underestimated at the nearshore GPS stations by HET_OPEN (Figure 8g), while such underestimation is not present in the HET_CLOSED solution (Figure 8h). The latter consistently recovers coastal vertical displacements with minimal errors (mean ~0.05 m or ~6%) (Figures 9f, 10f, and S4f), whereas the former underestimates nearshore d_z, particularly near Oregon by up to 0.8 m (Figures 9e, 10e, and S4e). The HET_OPEN-modeled $|h_{\max}|$ does not fit with the actual values by a

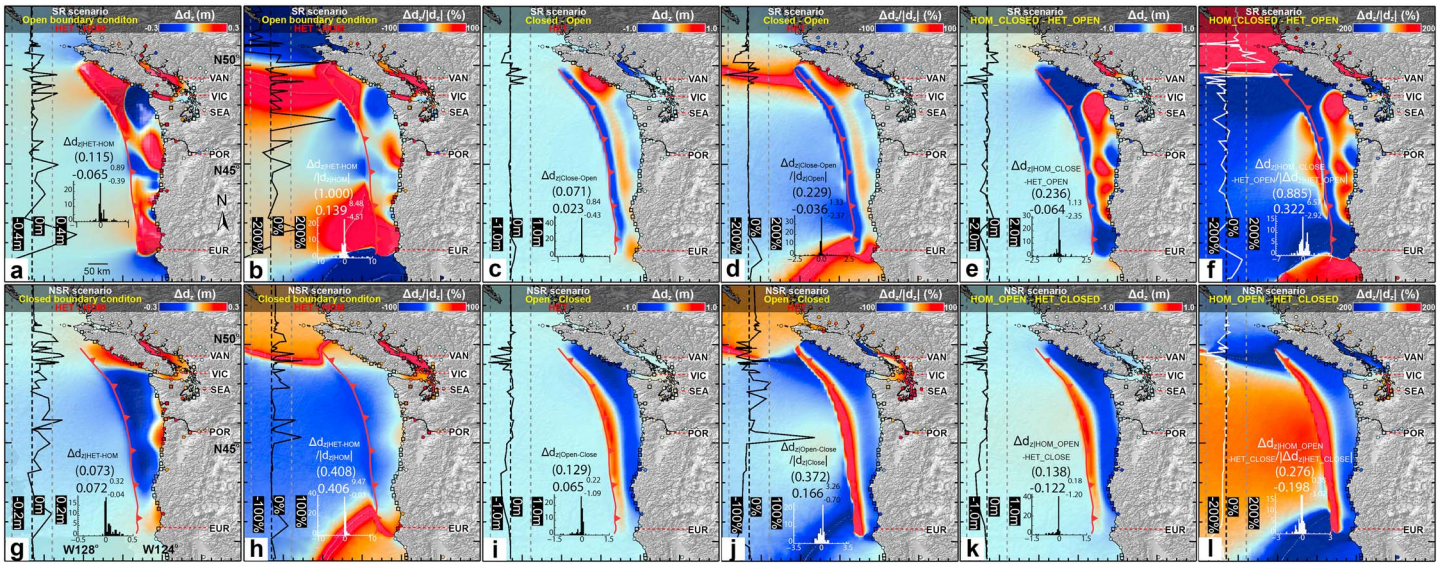

Figure 13. Comparison of inverted seafloor deformation among solutions by different inversion schemes for surface-rupturing (SR) and nonsurface-rupturing (NSR) scenarios. Difference, $\Delta d_{z|\text{HET-HOM}}$, and difference percentage, $\Delta d_{z|\text{HET-HOM}}/d_{z|\text{HOM}}$, between seafloor deformation inverted in heterogeneous (HET) and homogeneous (HOM) are shown for (a and b) SR and (g and h) NSR scenarios. Similarly, difference and difference percentage between solutions inverted with open and closed trench-rupture boundary conditions in HET are shown for (c and d) SR, $\Delta d_{z|\text{close-open}}$, and (i and j) NSR scenario, $\Delta d_{z|\text{open-closed}}$. Furthermore, difference, (e) $\Delta d_{z|\text{HOM\_CLOSED-HET\_OPEN}}$, (k) $\Delta d_{z|\text{HOM\_OPEN-HET\_CLOSED}}$, and difference percentage, (f) $\Delta d_{z|\text{HOM\_CLOSED-HET\_OPEN}}/d_{z|\text{HET\_OPEN}}$, (l) $\Delta d_{z|\text{HOM\_OPEN-HET\_CLOSED}}/d_{z|\text{HET\_CLOSED}}$, between solutions inverted by contradicting domain and rupture boundary conditions are shown for (e and f) SR and (k and l) NSR scenarios. Inverted seafloor deformation deviates by (a, b, g, and h) $|\Delta d_{z|\text{HET-HOM}}|_{\text{mean}}$ ~0.1 m and $|\Delta d_{z|\text{HET-HOM}}/d_{z|\text{HOM}}|_{\text{mean}}$ ~40–100% between HET and HOM for both scenarios. (a, b, g, and h) HET tends to produce larger coastal uplift than HOM along the coast of Pacific Northwest. Inverted d_z deviates by (c, d, i, and j) $|\Delta d_z|_{\text{mean}}$ ~0.1 m and $|\Delta d_z/d_z|_{\text{mean}}$ ~23–37% between solutions of open and closed rupture boundary conditions for both scenarios. (c, d, i, and j). Results of closed rupture boundary conditions tend to produce wider coastal uplift than those of open rupture boundary conditions along the coast of Pacific Northwest. Inverted seafloor deformation deviates by (e, k, f, and l) $|\Delta d_z|_{\text{mean}}$ ~0.2 m and $|\Delta d_z/d_z|_{\text{mean}}$ ~28–89% when inverting with both incompatible domain and rupture boundary conditions simultaneously.

mean error of 0.27 m (or ~37%) (Figures 11e, 12e, and S5e) >20 times larger than that (0.01 m or ~10%) of HET_CLOSED (Figures 11f, 12f, and S5f). The t_{hmax} of HET_CLOSED (Figure S7e) provide a closer estimate to actual h_{max} arrivals ($|\Delta t_{\text{hmax}}|_{\text{mean}}$~16 min) as compared to the solution of HET_OPEN ($|\Delta t_{\text{hmax}}|_{\text{mean}}$~20 min) especially near the coast of Washington and Oregon (Figures S7e and S7f). Similar observations are found when directly comparing HET_CLOSED and HET_OPEN solutions (Figures 13i and 13j and 14i and 14j). These results delineate the sensitivity of tsunami calculation toward different boundary conditions.

5. Discussion

It is well known that the simulation of tsunami wave profiles is sensitive to the earthquake slip distribution and fault geometry, as these two factors empirically control the seafloor deformation for tsunami genesis (Fujii et al., 2011; Goda et al., 2014; MacInnes et al., 2013; Satake et al., 2013; Ulutas, 2013; Wei et al., 2014). The transformation from spontaneous seismic energy outburst to permanent seafloor displacement is further complicated by the spatially varying material properties beneath the seafloor surface (Kyriakopoulos et al., 2013; Masterlark & Hughes, 2008; Tung & Masterlark, 2016). Softer materials usually encourage more deformation, while more rigid rocks remain surface intact (Tung & Masterlark, 2016). This directly influences how much potential energy is received by the offshore water body for generating tsunami waves, given a particular amount of seismic moment. Our results confirm that the inclusion of crustal heterogeneity in elastic models is essential for better estimates of seafloor deformation (Figures 3, 9, and 10) and tsunami propagation (Figures 5, 11, and 12). For both the SR and NSR scenarios, the solutions of inverse and forward analysis reveal a high prediction error (~14–20%) of h_{max} in HOM (Figures 5c and 5f and 10c and 10h) at least 4 times larger than that (error < 3.1%) in HET (Figures 12a and 12f). Such high error level is compatible with those (~20%) of the previous studies comparing Okada-based against FEM-based slip solutions of the 2009 L'Aquila earthquake (Trasatti et al., 2011) and Hikurangi slow events (Williams & Wallace, 2015).

For the forward analysis, the solutions of HET are distinguishable from those of HOM (Figure 3). Erroneous predictions of nearshore seafloor deformation by HOM can vary by up to 0.2 m (~20%) at some localities

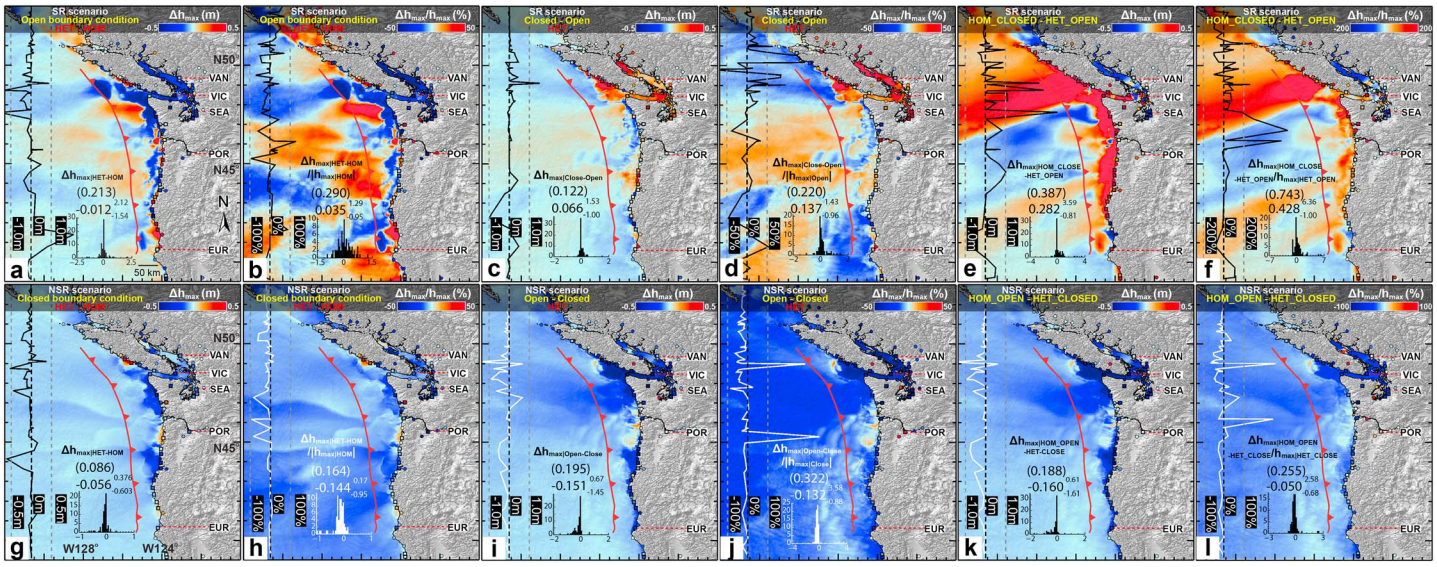

Figure 14. Comparison of estimated maximum tsunami height among solutions by different inversion schemes for surface-rupturing (SR) and nonsurface-rupturing (NSR) scenarios. Difference, $\Delta h_{\max|\text{HET-HOM}}$, and difference percentage, $\Delta h_{\max|\text{HET-HOM}}/h_{\max|\text{HOM}}$, between maximum tsunami height inverted in heterogeneous (HET) and homogeneous (HOM) are shown for (a and b) SR and (g and h) NSR scenarios. Similarly, difference and difference percentage between solutions inverted with closed and open trench-rupture boundary conditions in HET are shown for (c and d) SR, $\Delta h_{\max|\text{closed-open}}$, and (i and j) NSR scenario, $\Delta h_{\max|\text{open-closed}}$. Furthermore, difference, (e) $\Delta h_{\max|\text{HOM\_CLOSE-HET\_OPEN}}$, (k) $\Delta h_{\max|\text{HOM\_OPEN-HET\_CLOSED}}$, and difference percentage, (f) $\Delta h_{\max|\text{HOM\_CLOSE-HET\_OPEN}}/h_{\max|\text{HET\_OPEN}}$, (l) $\Delta h_{\max|\text{HOM\_OPEN-HET\_CLOSE}}/h_{\max|\text{HET\_CLOSED}}$, between solutions inverted with contradicting domain and rupture boundary conditions are shown for (e and f) SR and (k and l) NSR scenario. Estimated maximum tsunami heights deviate by (a, b, g, and h) $|\Delta h_{\max|\text{HET-HOM}}|_{\text{mean}}$ ~0.1–0.2 m and $|\Delta h_{\max|\text{HET-HOM}}/h_{\max|\text{HOM}}|_{\text{mean}}$ ~16–29% between HET and HOM for both scenarios. (a, b, g, and h) HET tends to estimate smaller $h_{\max}$ than HOM in Vancouver-Seattle area, while polarity of $\Delta h_{\max|\text{HET-HOM}}$ alternates along the coast of Pacific Northwest. Similarly, $h_{\max}$ deviates by (c, d, i, and j) $|\Delta h_{\max}|_{\text{mean}}$ ~0.12–0.2 m and $|\Delta h_{\max}/h_{\max}|_{\text{mean}}$ ~22–32% between solutions of open and closed rupture boundary conditions for both scenarios. (c, d, i, and j) Results of closed rupture boundary conditions tend to produce larger $\Delta h_{\max}$ than those of open rupture boundary condition. Furthermore, $h_{\max}$ deviates by (e, f, k, and l) $|\Delta d_z|_{\text{mean}}$ ~0.2–0.4 m and $|\Delta d_z/d_z|_{\text{mean}}$ ~26–74% when comparing models of incompatible domain and rupture boundary conditions for both scenarios simultaneously.

(Figure 3) attributable to the oversimplified elastic models, leading to different extent of tsunamic impact ($\Delta h_{\max}$ varying between −0.75 and 0.4 m) (Figures 5b and 5e) and arrival (Figures S1b and S1e). Regarding the lithospheric material of the CSZ, HET slip models of HET tend to give excessive seafloor uplift in the downdip direction of the main asperity and additional subsidence in the updip direction (Figures 3c and 3f), which is also true for the uniformly slipping model (Figure 4c). Such differential seafloor movements alter the signatures of tsunami waves being generated as well as the coastal vertical movements. However, the corresponding interpretation toward the coastal tsunami impact is not trivial and varies depending on the specific scenario. For instance, as deeper moment shows less seafloor movements over the offshore uplifting zone in HET (Figure 3f), less potential energy is transferred to the water body, and hence, HET generally gives rise to smaller $h_{\max}$ (blue domain of Figures 5e and 5f). On the contrary, for the trench-breaking rupture, larger values of $h_{\max}$ are generally obtained (though with spare local exceptions near Olympic Peninsula) by HET (Figures 5b and 5c) with additional seafloor uplift found near the shore (Figure 3c).

The HET-HOM solution discrepancy can be viewed as a (nonlinear) coupling effect between the seismic sources and the crustal complexity across the subduction boundary (Kyriakopoulos et al., 2013; Masterlark & Hughes, 2008). Increasing material heterogeneity translates to increasing differences between HET and HOM predictions for a range of scenarios (Figures 3 and 5). Due to computational inefficiency and tomography data resolution, HET is composed of only 1 million elements. However, the actual crustal domain, in reality, can be envisioned as an FEM with an infinite number of elements carrying different elastic properties. The predicted deformation from subduction slip is presumably a function of the resolution of the heterogeneity and should be radically different in HOM. This suggests the need for future assessments that identify sensitivities to the resolution of material complexity and, ideally, identify maximum mesh resolution thresholds. Accordingly, a finer grid of bathymetry and tsunami models (e.g., ~30 arcsec) could also be used to scrutinize the tsunami behavior in greater details. However, such tests of resolution are beyond the scope of this work.

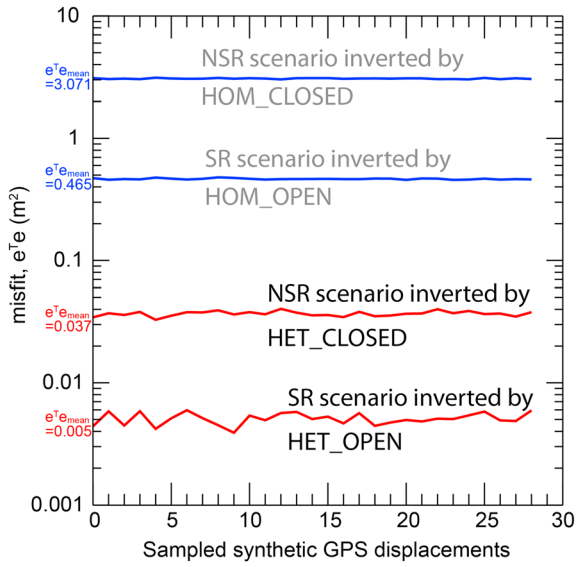

Figure 15. Model misfit versus multiple (30) sets of synthetic Global Positioning System displacements inheriting uncertainties (σ = 10%) of the *p* wave velocity in the seismic tomography model. The surface-rupturing and nonsurface-rupturing scenarios are inverted alternatively by G_{HET} and G_{HOM} with compatible boundary conditions. Better solutions are obtained by G_{HET} for both scenarios with model misfit 2–3 orders of magnitude smaller than those by G_{HOM}.

In addition to the model resolution, the uncertainties inherited in the seismic tomography model could also alter the material definition of the FEM domain and contribute to a different source solution. Our synthetic GPS data are generated in the HET model and best resolved in the inverse analysis of the similar domain (Figure 8). It is prompted to ask whether this still holds if the crustal domain synthetizing the GPS movements deviates from the HET model of G matrix, which is always the case for certain degree of tomographic uncertainties. Masterlark et al. (2016) demonstrate a pioneer study of studying how tomographic uncertainties (~10%) of velocity models propagate into the *G* matrix and then to the solutions of geodetic inversion. By inverting the surface deformation caused by the chamber pressurization of the Okmok volcano, Alaska, they found that the contribution of the uncertainties of a seismic tomography model is negligible (at 99% confidence) as compared to the difference between the HOM and HET model. We expect that similar phenomenon should exist for the seismic-source inversion here. To test this hypothesis, we generate 30 sets for synthetic GPS data of both the SR and NSR scenarios. Each data set is forward calculated by the velocity model with 1-sigma uncertainty of 10% in the *p* wave velocity. Each set of synthetic GPS data is generated by a new HET model whose crustal material (i.e., Young's Modulus) is altered by randomly perturbing the *p* wave velocity by 10% from its original value following a Gaussian distribution. This simulates the cases in which the actual crustal domain hosting the earthquake slip deviates from the HET models we impose in G_{HET}, which is very likely to be present in the field. We then invert these 60 sets (SR and NSR scenarios) of synthetic data by the original G_{HET} and G_{HOM} with compatible boundary conditions. The SR scenario is inverted by HET_OPEN and HOM_OPEN, respectively, while the NSR scenario is inverted by HET_CLOSED and HOM_CLOSED, respectively (Figure 15). Such approach provides a statistically sound comparison on the effectiveness of each inversion scheme, as the models generating synthetic GPS data are no longer identical to those of the inverse analysis. Such stochastic analysis shows that the inversion using G_{HET} always gives a significantly better solution than that using G_{HOM} at 99% confidence (Figure 15), as the *F*-ratio test indicates that the *F*-ratio = $e^Te_{HOM}/e^Te_{HET} > 100$ is always greater than the $F_{threshold}$ = 1.23 at 99% confidence. The data misfits inverted by G_{HET}, 0.004–0.006 m^2 for the SR scenario and 0.03–0.04 m^2 for the NSR scenario, are drastically smaller by 2 orders of magnitude than those by G_{HOM} range between 0.46 and 0.48 m^2 for the SR scenario and 3.04 and 3.12 m^2 for the NSR scenario (Figure 15). Moreover, the misfit difference between the SR and NSR solutions implies that the prediction accuracy varies with different slip patterns. The SR scenario is typically better resolved with 10-time smaller misfit values than the NSR scenario (Figure 15). Collectively, this result reaffirms that the deviation of crustal materials expected for tomography uncertainties does not alter the superiority of G_{HET} in resolving a more accurate slip distribution. However, we understand that the scenarios of our study are the ideal cases of megathrust rupture which can involve more complex smaller wavelength slip patterns. Therefore, future studies are encouraged to investigate the solution invariability toward velocity-model uncertainties for a wider range of earthquake scenarios.

Studying the sensitivity of tsunami forecasts to material assumptions can be also cast in the framework of a linear inverse problem resolving the surface condition for modeling tsunami, as aforementioned in equation (1). Generally, prediction errors, e^Te, of coseismic GPS movements are significantly larger (~1,000 times) when inverting with G_{HOM} (Figures 8d, 8e, 8i, and 8j) over G_{HET} (Figures 8b, 8c, 8g, and 8h), regardless of rupture boundary conditions. The prediction differences for tsunamis between HET and HOM solutions are amplified in the inverse analyses (Figures 8–15) by two calculation steps which could introduce the domain uncertainties of HOM into the final tsunami estimations (Figure 12). First, the seismic sources inverted by HOM may inherit a certain amount of errors represented by unrealistic slip characteristics (Figures 8d and 8e). Since the Green's function matrix of HOM does not honor the nonuniform rock material which translates slips to GPS displacements on the surface, the linear solutions of the incompatible elastic domain were

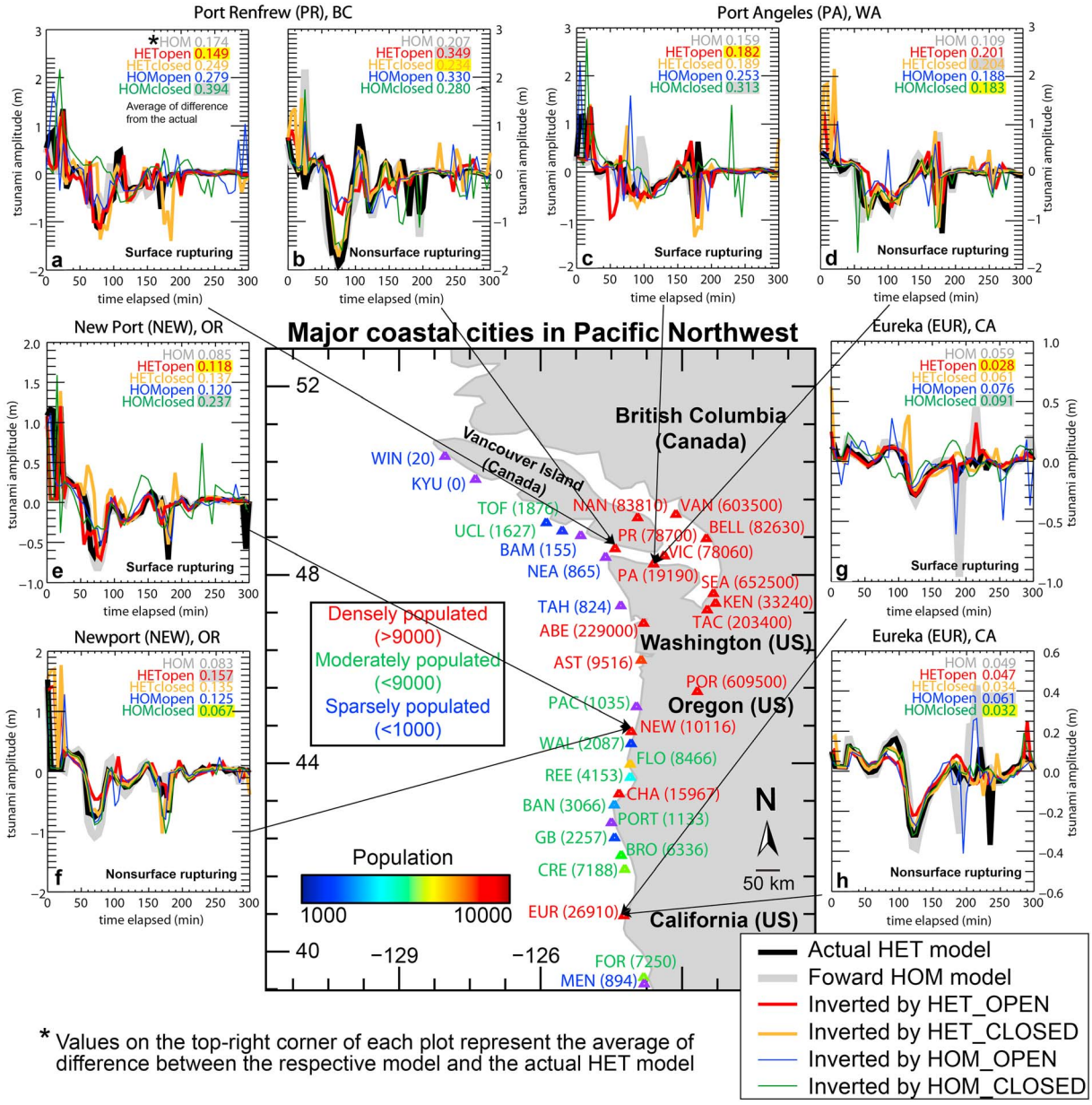

Figure 16. Comparison of estimated tsunami waveform computed from different inversion schemes for surface-rupturing (SR) and nonsurface-rupturing (NSR) scenarios. The map (center) shows (red) densely, (green) moderately, and (blue) sparsely populated cities along the coast of Pacific Northwest where host a population of 3 million. The label color of city name refers to the population categorization, and the triangle color denotes local population (also shown in brackets). Time series of tsunami waveforms are studied in four densely populated cities, namely, (a and b) Port Renfrew (British Columbia), (c and d) Port Angeles (Washington), (e and f) Newport (Oregon), and (g and h) Eureka (California). Given (Figure 7a) SR and (Figure 7f) NSR slip distribution, actual/reference tsunami amplitude is simulated in heterogeneous (HET) for (a, c, e, and g) SR and (b, d, f, and h) NSR scenarios, as shown by black lines. The counterpart simulations in homogeneous (HOM) are shown as gray lines. For each city, tsunami time series are compared among predictions derived from different inversion schemes, namely, HET_OPEN (red line), HET_CLOSED (orange line), HOM_OPEN (blue line), and HOM_CLOSED (green line). The top-right box of each subfigure shows the mean of discrepancy between corresponding predictions and the actual model. The yellow shades and gray shades designate the best and worst inversion schemes in terms of prediction-actual misfits, respectively.

"forced" to fit the observations (Figures 8d and 8j). Artifacts are then introduced to these slip solutions jeopardized by, for example, alternative-reverse-normal mechanisms which are not mechanically plausible (Figures 8d and 8e). Therefore, seafloor movements inverted in (Figures 10c, 10d, 10g, and 10h) HOM generally attain larger misfits ($0.07\ \text{m} < |\Delta d_z|_{\text{mean}} < 0.21\ \text{m}$) than those in (Figures 10a, 10b, 10e, and 10f) HET ($0.03\ \text{m} < |\Delta d_z|_{\text{mean}} < 0.12\ \text{m}$). The tsunami formation, as a result, cannot be satisfactorily recovered in HOM (Figures 12a, 12b, 12e, and 12f). Those nonrealistic slip characteristics and deformation are common

in the solutions of linear analyses using analytical HOM solutions (Okada, 1985) and usually removed or suppressed by additional constraints such as nonnegativity constraints (Du et al., 1992). However, this problem is not seen in HET, which does not require a slip-positivity constraint to derive physically sound solutions (Figures 8b and 8h) (cf. Hudnut et al., 1996). This highlights the advantage of HET on resolving seismic sources over the half-space models (Kyriakopoulos et al., 2013; Tung & Masterlark, 2016). Second, additional uncertainties are imparted into the tsunami sources when simulating seafloor deformation from the spurious inverse solutions through a HOM-based forward model. Disrupted by the numerical artifacts in the slip solutions of HOM (Figures 8d and 8e), the estimated seafloor deformation adds another suite of uncertainties to the tsunami source when the uniform crust oversimplifies the deformation signals on the seabed, as shown by the results of forward analyses (Figures 3, 4, and 5). Through these two steps, fallacious seafloor movements are developed for tsunami excitation (Figures 9c, 9d, 10c, 10d, S4c, and S4d). As a result, forecasted tsunami impact calculated in (Figures 12c, 12d, 12g, and 12h) HOM generally attain larger uncertainties ($0.14\ \text{m} < |\Delta h_{\max}|_{\text{mean}} < 0.38\ \text{m}$) than those in (Figures 12a, 12b, 12e, and 12f) HET ($0.03\ \text{m} < |\Delta h_{\max}|_{\text{mean}} < 0.27\ \text{m}$). For the case of the SR scenario inverted by HOM_OPEN, near-trench seafloor subsidence (up to 3 m) and uplift (>3 m near Vancouver Island) are mistakenly simulated on the hanging block of megathrust zones (Figures 9c and 10c), leading to discernible errors of forecasted tsunami height ($-1.6 < \Delta h_{\max} < 1.6\ \text{m}$ or $|\Delta h_{\max}/|h_{\max}||_{\text{mean}} \sim 36\%$) (Figures 11c, 12c, and S5c). Those large-scale errors are not found with the HET_OPEN inversion solutions which show consistent (>90%) prediction of d_z and $h_{\max}$ with accuracy better than 0.3 m (Figures 9a, 10a, 11a, and 12a). Based on these results, we accept the hypothesis that the near-field tsunami forecast is significantly sensitive to the domain definition of geodetic inverse analyses.

Another important requirement for accurately resolving the seismic and tsunami sources is to adopt appropriate boundary conditions in the inverse analysis (equation (1)). The fault-top boundary conditions determine whether the solutions are NSR or SR by shifting the vertical location of slip asperities and suppressing/encouraging near-trench slips. As these mechanisms deform the near-field area differently even with same magnitude (Figures 3b and 3e and 9a and 9f), we expect they should contribute to different predictions of tsunami dynamics and coastal subsidence/uplift, which is also supported by Goda et al. (2014) and Ulutas (2013). Satake et al. (2013) found distinguishable tsunami behaviors triggered by deep and shallow slips. They point out that a near-trench rupture is typically responsible for the larger impulsive tsunami amplitude along the coast, while deeper subfault offsets encourage an earlier wave arrival but with gradual sea level rise. Such observations generally agree with our results (Figures 7 and S2).

For near-field tsunami hazards, the NSR mechanism usually creates more coast uplift by ~0.1 m (~20%) than the SR slips (Figure 6). Their estimated $h_{\max}$ could differ by up to 1.6 m (~130%) (Figures 7a and 7b). As expected by Satake et al. (2013), the $h_{\max}$ of the NSR scenario arrives ~10 min earlier than that of the SR scenario (Figure S2a). For an inverse analysis, using inappropriate boundary conditions for the rupture surface to invert a seismic source always results in incompatible solutions (Figures 8c, 8e, 8g, and 8i). The solutions of mismatched boundary conditions often provide misleading estimates of locations (deviate by few 100 km) and slip magnitude of the major asperity (Figures 8c and 8g). Failure of imposing closed rupture boundary condition to invert for the NSR slip propagates slips near trench (Figures 8g and 8i), ending up with underestimated GPS movements ($\mathbf{e}^{\mathrm{T}}\mathbf{e} > 13\ \text{m}^2$) along the coast in comparison with the results ($\mathbf{e}^{\mathrm{T}}\mathbf{e} < 3.4\ \text{m}^2$) of compatible trench-rupture boundary conditions (Figures 8h and 8j). Similarly for the SR scenario, most slips (max. ~16 m) are correctly resolved near the trench at 47°N in HET_OPEN (Figure 8b), whereas HET_CLOSED concentrates high moment (max. ~13 m) deeper at 49°N (Figure 8c). Similarly for the NSR scenario, most slips (max ~12 m) are properly imaged deeper at 48°N in HET_CLOSED (Figure 8h), while HET_OPEN allows nonrealistic shallow moment (max ~11 m) clustered near the trench at 46°N (Figure 8g). Uncertainties of the estimated vertical displacements ($|\Delta d_z|$ up to 1 m or ~100%) (Figures 10b, 10e, S4b, and S4e) are transferred to that of maximum wave height causing coastal $\Delta h_{\max}$ up to 3.2 m (Figures 12b, 12e, S5b, and S5e). These uncertainties are at least 2 times larger than those of solutions constrained with compatible trench-rupturing boundary ($|\Delta d_z| < 0.5\ \text{m}$, $\Delta h_{\max} < 1.7\ \text{m}$) (Figures 10a, 10f, 12a, and 12f). Regional miscalculation of $h_{\max}$ is the smallest when SR and NSR scenarios are inverted by (Figure 12a) HET_OPEN and (Figure 12f) HET_CLOSED, respectively. Therefore, the near-field tsunami behavior can only be precisely predicted when the near-trench slip behavior is properly interpreted and compiled in the slip-boundary condition of inverse analysis. The real-time determination of whether a megathrust rupture reaches the trench is nearly impossible due to the

inaccessible deep-marine environment and inadequate seafloor instrumentation. Hence, we suggest using the inversion solutions of both HET_OPEN and HET_CLOSED as end-members to outline a range of possible tsunami behaviors. During tsunamigenic events, we expect that the actual tsunami observations from the offshore sea level monitoring, nearshore GPS buoys, and coastal tide gauges fall into this range or at least not far from it and meanwhile updates the source information retrospectively. For an early stage (first 30 min) before the waves arrive at the coast, these two solutions should present a plausible range of displacement fields (Figures 9a, 9b, 9e, and 9f), coastal h_{max} (Figures 11a, 11b, 11e, and 11f), and Δt_{hmax} (Figures S6a, S6b, S6e, and S6f) for evaluating tsunami hazard.

The prediction accuracy of tsunami sources further deteriorates when both the domain definition and boundary conditions of the slip inversion significantly deviate from the actual crustal and seismic configurations (Figures 8e, 8i, S4d, and S4g). For the SR scenario solved by HOM_CLOSED, a large-scale numerical artifact of normal faulting ($>$14 m) occurs near the Vancouver Island and Northern California (Figure 8e) and causes unrealistic seafloor subsidence ($>$3 m) in the vicinity (Figures 9d and 10d). Compared with the solutions of other inversion schemes (Figures 12a–12c), HOM_CLOSED creates significantly more uncertainties (up to 3.7 m) of the predicted h_{max} both onshore and offshore (Figure 12d). In this case, the worst predictions of d_z (Figure 10d), h_{max} (Figure 12d), and t_{hmax} (Figure S7d) are observed. In a forecasting prospective, we directly compare the solutions of HET_OPEN against HOM_CLOSED for the SR scenario (Figures 13e and 13f, 14e and 14f, and 15e and 15f) and those of HET_CLOSED against HOM_OPEN for the NSR scenario (Figures 13k and 13l, 14k and 14l, and 15k and 15l). It is clear that inverting with simultaneously incompatible domain and boundary conditions yields the worst predictions of d_z, h_{max}, and t_{hmax} among other inversion schemes, severely reducing the reliability of the corresponding hazard assessments. For seismic inversions, Green's functions of velocity models (e.g., CRUST2.0), which depict the signatures of seismic wave propagation (Julian & Foulger, 1996), are widely adopted to invert the wave arrivals for source estimation (Newman et al., 2011; Shao et al., 2011; Tassara & Echaurren, 2012). It is generally accepted that the corresponding solutions could be benefited by a more compatible velocity model employed in the inverse analysis (Dreger & Helmberger, 1991; Liu et al., 2004). Therefore, we anticipate that similar solution sensitivity to domain configurations exists when inverting the seismic data, but such analysis is beyond the scope of this study.

Furthermore, we study the sensitivity of tsunami forecasts to various inversion schemes by investigating the temporal tsunami wave profiles at several populated cities along the Pacific Northwest coast (Figure 16). These cities include Port Renfrew (British Columbia, Canada), Port Angeles (Washington, USA), Newport (Oregon, USA), and Eureka (California, USA). The temporal evolutions of coastal wave heights from both SR and NSR scenarios are predicted over these cities. The predictions are compared against the actual (HET) models serving as a reference. Fundamental differences of amplitude time series are observed between the actual HET (black lines in Figure 16) and the HOM (gray lines in Figure 16) models, which is consistent with our findings in the forward analysis (Figure 5). For an SR event, the wave profiles at four cities are particularly better predicted ($0.03 < \text{misfit}_{mean} < 0.2$ m^2) when the inverse analysis adopts an HET domain and an open boundary condition (Figures 16a, 16c, 16e, and 16g). The solutions of HET_OPEN (red lines in Figure 16) largely recover the actual waveform (black lines in Figure 16) as benchmarked by comparable h_{max} and t_{hmax}. The predictions degrade (increased misfit_{mean} up to 0.1 m) when applying an incompatible boundary condition (orange lines in Figures 16a, 16c, 16e, and 16g) and deteriorate when considering a mechanically uniform crust (blue lines in Figures 16a, 16c, 16e, and 16g). The worst solutions are consistently found when both crustal domain and boundary condition are incompatible with the reference model (green lines in Figures 16a, 16c, 16e, and 16g). However, the results for NSR scenario are less consistent (Figures 16b, 16d, 16h, and 16f). The best fit predictions are not necessarily calculated from the settings of a compatible domain and boundary condition. This can be ascribed to the aforementioned unsatisfactory slip resolutions distorted by the uneven distribution of the GPS network (Figure 1) (cf. Masterlark et al., 2001).

6. Conclusions

The aim of this study is to demonstrate the sensitivity of near-field tsunami forecasts toward the HET crustal domain and boundary conditions of (forward and inverse) deformation analysis. Tsunami impact is studied along the coast of Pacific Northwest. The importance of material and surface-slipping configuration is particularly highlighted when the coseismic deformation is inverted with spatially uniform elastic models and

incompatible updip slip boundary which lead to implausible source characteristics and significantly corrupt the tsunami hazard assessments. A stochastic analysis confirms that the HET inversion regime is significantly better in recovering the synthetic GPS displacements than the HOM regime for the earthquake scenarios we study, even when there are tomographic uncertainties inherited in the synthetic GPS data. Applying compatible boundary conditions is critical as a nontrench-breaking rupture tends to deform the coast more and cause earlier wave arrivals than a trench-breaking one. These results are important to improve the prediction accuracy of near-field tsunami warning systems which initially rely on the inverse analysis of timely available geodetic or seismic data for source calibration before the gigantic waves reach the shore upon a tsunamigenic earthquake. Keeping abreast of the increasing coverage of geodetic networks, the detailed configurations of elastic deformation and inverse analysis are essential for simulating the crustal material complexity and hence imaging megathrust rupture. We expect the study of model configurations to be extended to other subduction boundaries for studying the similar hazards. For more reliable tsunami forecasts, future studies should further improve the resolutions of FEM and hydraulic modeling grids with higher-definition topography/bathymetry and tomography data, to better quantify the variability of coastal impact for various tsunami-earthquake scenarios, as well as any local effects due to irregular coastline geometry.

Acknowledgments
This material is based upon work supported by the National Science Foundation under grant 1316082. This work is also supported, in part, by NASA grant NNX17AD96G and NASA ESI grant 16-ESI16-0038. Academic licensing and technical support for Abaqus software was provided by Dassault Systèmes Simulia Corp. We thank Tim Melbourne for providing the real-time GPS data and station information and express our gratitude to Xiaoming Wang for sharing the COMCOT tsunami modeling software. The data used are listed in the references, tables, and supplements.

References

Amante, C., & Eakins, B. W. (2009). ETOPO1 1 Arc-Minute Global Relief Model: Procedures, Data sources and analysis, US Department of Commerce, National Oceanic and Atmospheric Administration, National Environmental Satellite, Data, and Information Service, National Geophysical Data Center, Marine Geology and Geophysics Division Colorado.

Ammon, C. J., Lay, T., Kanamori, H., & Cleveland, M. (2011). A rupture model of the 2011 off the Pacific coast of Tohoku earthquake. *Earth, Planets and Space*, *63*(7), 693–696. https://doi.org/10.5047/eps.2011.05.015

Aster, R. C., Borchers, B., & Thurber, C. H. (2011). *Parameter estimation and inverse problems*. Cambridge, MA: Academic Press.

Atwater, B. F. (1987). Evidence for great Holocene earthquakes along the outer coast of Washington State. *Science*, *236*(4804), 942–944. https://doi.org/10.1126/science.236.4804.942

Austin, K., Blume, F., Berglund, H., Dittman, T., Feaux, K., Gallaher, W., et al. (2013). The Plate Boundary Observatory Cascadia Network: Development and installation of a large scale real-time GPS network. Abstract G53B-0931 Presented at the 2013 AGU Fall Meeting, San Francisco, CA.

Bartlow, N. M., Miyazaki, S. I., Bradley, A. M., & Segall, P. (2011). Space-time correlation of slip and tremor during the 2009 Cascadia slow slip event. *Geophysical Research Letters*, *38*, L18309. https://doi.org/10.1029/2011GL048714

Bassin, C., Laske, G., & Masters, G. (2000). The current limits of resolution for surface wave tomography in North America. *Eos*, *81*.

Bjarnason, I. T., Menke, W., Flóvenz, Ó. G., & Caress, D. (1993). Tomographic image of the mid-Atlantic plate boundary in southwestern Iceland. *Journal of Geophysical Research*, *98*(B4), 6607–6622. https://doi.org/10.1029/92JB02412

Blewitt, G., Hammond, W. C., Kreemer, C., Plag, H.-P., Stein, S., & Okal, E. (2009). GPS for real-time earthquake source determination and tsunami warning systems. *Journal of Geodesy*, *83*(3–4), 335–343. https://doi.org/10.1007/s00190-008-0262-5

Calvert, A. J., Preston, L. A., & Farahbod, A. M. (2011). Sedimentary underplating at the Cascadia mantle-wedge corner revealed by seismic imaging. *Nature Geoscience*, *4*(8), 545–548. https://doi.org/10.1038/ngeo1195

Clague, J. J. (1997). Evidence for large earthquakes at the Cascadia subduction zone. *Reviews of Geophysics*, *35*(4), 439–460. https://doi.org/10.1029/97RG00222

Dragert, H., Wang, K., & James, T. S. (2001). A silent slip event on the deeper Cascadia subduction interface. *Science*, *292*(5521), 1525–1528. https://doi.org/10.1126/science.1060152

Dreger, D., & Helmberger, D. (1991). Source parameters of the Sierra Madre earthquake from regional and local body waves. *Geophysical Research Letters*, *18*(11), 2015–2018. https://doi.org/10.1029/91GL02366

Du, Y., Aydin, A., & Segall, P. (1992). Comparison of various inversion techniques as applied to the determination of a geophysical deformation model for the 1983 Borah Peak earthquake. *Bulletin of the Seismological Society of America*, *82*(4), 1840–1866.

Eleonora, R., Walter, M., & Maurizio, B. (2002). The edge dislocation problem in a layered elastic medium. *Geophysical Journal International*, *149*(2), 508–523.

Fernandez, J., Yu, T. T., & Rundle, J. B. (1996). Deformation produced by a rectangular dipping fault in a viscoelastic-gravitational layered Earth model. 1. Thrust fault - FLTGRV and FLTGRH FORTRAN programs. *Computers & Geosciences*, *22*(7), 735–750.

Fujihashi, K., Aoki, T., Okutsu, M., Arai, K., Komori, T., Fujita, H., et al. (2007). Development of seafloor seismic and tsunami observation system, paper presented at Underwater Technology and Workshop on Scientific Use of Submarine Cables and Related Technologies, 2007. Symposium on, IEEE.

Fujii, Y., & Satake, K. (2007). Tsunami source of the 2004 Sumatra-Andaman earthquake inferred from tide gauge and satellite data. *Bulletin of the Seismological Society of America*, *97*(1A), S192–S207. https://doi.org/10.1785/0120050613

Fujii, Y., Satake, K., Sakai, S. I., Shinohara, M., & Kanazawa, T. (2011). Tsunami source of the 2011 off the Pacific coast of Tohoku Earthquake. *Earth, Planets and Space*, *63*(7), 55.

Gao, X., & Wang, K. (2017). Rheological separation of the megathrust seismogenic zone and episodic tremor and slip. *Nature*, *543*(7645), 416–419. https://doi.org/10.1038/nature21389

Geist, E. L. (2005). Local tsunami hazards in the Pacific Northwest from Cascadia Subduction Zone earthquakes, US Dept. of the Interior, US Geological Survey.

Goda, K., Mai, P. M., Yasuda, T., & Mori, N. (2014). Sensitivity of tsunami wave profiles and inundation simulations to earthquake slip and fault geometry for the 2011 Tohoku earthquake. *Earth, Planets and Space*, *66*(1), 105. https://doi.org/10.1186/1880-5981-66-105

González, F., Geist, E. L., Jaffe, B., Kânoğlu, U., Mofjeld, H., Synolakis, C., et al. (2009). Probabilistic tsunami hazard assessment at seaside, Oregon, for near-and far-field seismic sources. *Journal of Geophysical Research*, *114*, C11023. https://doi.org/10.1029/2008JC005132

Grilli, T., Harris, J. C., Bakhsh, T. S. T., Masterlark, T. L., Kyriakopoulos, C., Kirby, J. T., & Shi, F. (2013). Numerical simulation of the 2011 Tohoku tsunami based on a new transient FEM co-seismic source: Comparison to far-and near-field observations. *Pure and Applied Geophysics*, *170*(6-8), 1333–1359. https://doi.org/10.1007/s00024-012-0528-y

Gusman, A. R., Tanioka, Y., Sakai, S., & Tsushima, H. (2012). Source model of the great 2011 Tohoku earthquake estimated from tsunami waveforms and crustal deformation data. *Earth and Planetary Science Letters*, *341*, 234–242.

Gutscher, M. A., Spakman, W., Bijwaard, H., & Engdahl, E. R. (2000). Geodynamics of flat subduction: Seismicity and tomographic constraints from the Andean margin. *Tectonics*, *19*(5), 814–833. https://doi.org/10.1029/1999TC001152

Hayes, G. P. (2011). Rapid source characterization of the 2011 Mw 9.0 off the Pacific coast of Tohoku earthquake. *Earth, Planets and Space*, *63*(7), 4.

Hayes, G. P., Wald, D. J., & Johnson, R. L. (2012). Slab1.0: A three-dimensional model of global subduction zone geometries. *Journal of Geophysical Research*, *117*, B01302. https://doi.org/10.1029/2011JB008524

He, J., & Peltzer, G. (2009). Poroelastic triggering in the January 9–22, 2008 Nima-Gaize (Tibet) earthquake sequence, paper presented at AGU Fall Meeting Abstracts.

He, W., Wang, M., & Yao, Z. X. (2003). Static deformation due to shear and tensile faults in a layered half-space. *Bulletin of the Seismological Society of America*, *93*(5), 2253–2263. https://doi.org/10.1785/0120020136

Hoechner, A., Babeyko, A. Y., & Sobolev, S. V. (2008). Enhanced GPS inversion technique applied to the 2004 Sumatra earthquake and tsunami. *Geophysical Research Letters*, *35*, L08310. https://doi.org/10.1029/2007GL033133

Hudnut, K., Shen, Z., Murray, M., McClusky, S., King, R., Herring, T., et al. (1996). Co-seismic displacements of the 1994 Northridge, California, earthquake. *Bulletin of the Seismological Society of America*, *86*(1B), S19–S36.

Hughes, K. L. H., Masterlark, T., & Mooney, W. D. (2010). Poroelastic stress-triggering of the 2005 M8. 7 Nias earthquake by the 2004 M9. 2 Sumatra–Andaman earthquake. *Earth and Planetary Science Letters*, *293*(3-4), 289–299. https://doi.org/10.1016/j.epsl.2010.02.043

Iinuma, T., Ohzono, M., Ohta, Y., & Miura, S. (2011). Coseismic slip distribution of the 2011 off the Pacific coast of Tohoku earthquake (M 9.0) estimated based on GPS data—Was the asperity in Miyagi-oki ruptured? *Earth, Planets and Space*, *63*(7), 643–648. https://doi.org/10.5047/eps.2011.06.013

Iinuma, T., Hino, R., Kido, M., Inazu, D., Osada, Y., Ito, Y., et al. (2012). Coseismic slip distribution of the 2011 off the Pacific Coast of Tohoku Earthquake (M9. 0) refined by means of seafloor geodetic data. *Journal of Geophysical Research*, *117*, B07409. https://doi.org/10.1029/2012JB009186

Jovanovich, D. B., Husseini, M. I., & Chinnery, M. A. (1974). Elastic dislocations in a layered half-space—I. Basic theory and numerical methods. *Geophysical Journal International*, *39*(2), 205–217.

Julian, B. R., & Foulger, G. (1996). Earthquake mechanisms from linear-programming inversion of seismic-wave amplitude ratios. *Bulletin of the Seismological Society of America*, *86*(4), 972–980.

Kajiura, K. (1970). 45. Tsunami source, energy and the directivity of wave radiation, Earthquake Research Institute, University of Tokyo.

Kim, Y., Abers, G. A., Li, J., Christensen, D., Calkins, J., & Rondenay, S. (2014). Alaska Megathrust 2: Imaging the megathrust zone and Yakutat/Pacific plate interface in the Alaska subduction zone. *Journal of Geophysical Research: Solid Earth*, *119*, 1924–1941. https://doi.org/10.1002/2013JB010581

Kyriakopoulos, C., Masterlark, T., Stramondo, S., Chini, M., & Bignami, C. (2013). Coseismic slip distribution for the Mw 9 2011 Tohoku-Oki earthquake derived from 3-D FE modeling. *Journal of Geophysical Research: Solid Earth*, *118*, 3837–3847. https://doi.org/10.1002/jgrb.50265

Lee, S. (2012). Rupture process of the 2011 Tohoku-Oki earthquake based upon joint source inversion of teleseismic and GPS data. *Terrestrial, Atmospheric*, *23*(1), 1–7.

Liu, Q., Polet, J., Komatitsch, D., & Tromp, J. (2004). Spectral-element moment tensor inversions for earthquakes in southern California. *Bulletin of the Seismological Society of America*, *94*(5), 1748–1761. https://doi.org/10.1785/012004038

MacInnes, B. T., Gusman, A. R., LeVeque, R. J., & Tanioka, Y. (2013). Comparison of earthquake source models for the 2011 Tohoku event using tsunami simulations and near-field observations. *Bulletin of the Seismological Society of America*, *103*(2B), 1256–1274. https://doi.org/10.1785/0120120121

Masterlark, T. (2003). Finite element model predictions of static deformation from dislocation sources in a subduction zone: Sensitivities to homogeneous, isotropic, Poisson-solid, and half-space assumptions. *Journal of Geophysical Research*, *108*(2540), 1029–2510.

Masterlark, T., & Hughes, K. L. H. (2008). Next generation of deformation models for the 2004 M9 Sumatra-Andaman earthquake. *Geophysical Research Letters*, *35*, L19310. https://doi.org/10.1029/2008GL035198

Masterlark, T., DeMets, C., Wang, H., Sanchez, O., & Stock, J. (2001). Homogeneous vs heterogeneous subduction zone models: Coseismic and postseismic deformation. *Geophysical Research Letters*, *28*(21), 4047–4050. https://doi.org/10.1029/2001GL013612

Masterlark, T., Feigl, K. L., Haney, M., Stone, J., Thurber, C., & Ronchin, E. (2012). Nonlinear estimation of geometric parameters in FEMs of volcano deformation: Integrating tomography models and geodetic data for Okmok volcano, Alaska. *Journal of Geophysical Research*, *117*, B020407. https://doi.org/10.1029/2011jb008811

Masterlark, T., Donovan, T., Feigl, K. L., Haney, M., Thurber, C. H., & Tung, S. (2016). Volcano deformation source parameters estimated from InSAR: Sensitivities to uncertainties in seismic tomography. *Journal of Geophysical Research: Solid Earth*, *121*, 3002–3016. https://doi.org/10.1002/2015JB012656

McCaffrey, R., Qamar, A. I., King, R. W., Wells, R., Khazaradze, G., Williams, C. A., et al. (2007). Fault locking, block rotation and crustal deformation in the Pacific Northwest. *Geophysical Journal International*, *169*(3), 1315–1340. https://doi.org/10.1111/j.1365-246X.2007.03371.x

McCaffrey, R., King, R. W., Payne, S. J., & Lancaster, M. (2013). Active tectonics of northwestern US inferred from GPS-derived surface velocities. *Journal of Geophysical Research: Solid Earth*, *118*, 709–723. https://doi.org/10.1029/2012JB009473

Menke, W. (2012). *Geophysical data analysis: Discrete inverse theory*. Cambridge, MA: Academic Press.

Miller, M. M., Melbourne, T., Johnson, D. J., & Sumner, W. Q. (2002). Periodic slow earthquakes from the Cascadia Subduction Zone. *Science*, *295*(5564), 2423–2423. https://doi.org/10.1126/science.1071193

Momma, H., Fujiwara, N., Kawaguchi, K., Iwase, R., Suzuki, S., & Kinoshita, H. (2002). Monitoring system for submarine earthquakes and deep sea environment. Paper presented at OCEANS'97. MTS/IEEE Conference Proceedings, IEEE.

Newman, A. V., Hayes, G., Wei, Y., & Convers, J. (2011). The 25 October 2010 Mentawai tsunami earthquake, from real-time discriminants, finite-fault rupture, and tsunami excitation. *Geophysical Research Letters*, *38*, L05302. https://doi.org/10.1029/2010GL046498

Ohta, Y., Kobayashi, T., Tsushima, H., Miura, S., Hino, R., Takasu, T., et al. (2012). Quasi real-time fault model estimation for near-field tsunami forecasting based on RTK-GPS analysis: Application to the 2011 Tohoku-Oki earthquake (Mw 9.0). *Journal of Geophysical Research*, *117*, B02311. https://doi.org/10.1029/2011JB008750

Okada, Y. (1985). Surface deformation due to shear and tensile faults in a half-space. *Bulletin of the Seismological Society of America*, *75*(4), 1135.
Okal, E. A., & Synolakis, C. E. (2008). Far-field tsunami hazard from mega-thrust earthquakes in the Indian Ocean. *Geophysical Journal International*, *172*(3), 995–1015. https://doi.org/10.1111/j.1365-246X.2007.03674.x
Oleskevich, D., Hyndman, R., & Wang, K. (1999). The updip and downdip limits to great subduction earthquakes: Thermal and structural models of Cascadia, south Alaska, SW Japan, and Chile. *Journal of Geophysical Research*, *104*(B7), 14,965–14,991. https://doi.org/10.1029/1999JB900060
Ozawa, S., Nishimura, T., Suito, H., Kobayashi, T., Tobita, M., & Imakiire, T. (2011). Coseismic and postseismic slip of the 2011 magnitude-9 Tohoku-Oki earthquake. *Nature*, *475*(7356), 373–376. https://doi.org/10.1038/nature10227
Pan, E. (1999). Green's functions in layered poroelastic half-spaces. *International Journal for Numerical and Analytical Methods in Geomechanics*, *23*(13), 1631–1653. https://doi.org/10.1002/(SICI)1096-9853(199911)23:13%3C1631::AID-NAG60%3E3.0.CO;2-Q
Priest, G., Goldfinger, C., Wang, K., Witter, R., Zhang, Y., & Baptista, A. (2010). Confidence levels for tsunami-inundation limits in northern Oregon inferred from a 10,000-year history of great earthquakes at the Cascadia Subduction Zone. *Natural Hazards*, *54*(1), 27–73. https://doi.org/10.1007/s11069-009-9453-5
Rogers, G., & Dragert, H. (2003). Episodic tremor and slip on the Cascadia Subduction Zone: The chatter of silent slip. *Science*, *300*(5627), 1942–1943. https://doi.org/10.1126/science.1084783
Romano, F., Trasatti, E., Lorito, S., Piromallo, C., Piatanesi, A., Ito, Y., et al. (2014). Structural control on the Tohoku earthquake rupture process investigated by 3D FEM, tsunami and geodetic data. *Scientific Reports*, *4*, 5631. https://doi.org/10.1038/srep05631
Satake, K. (2014). Advances in earthquake and tsunami sciences and disaster risk reduction since the 2004 Indian ocean tsunami. *Geoscience Letters*, *1*(1), 15. https://doi.org/10.1186/s40562-014-0015-7
Satake, K., Fujii, Y., Harada, T., & Namegaya, Y. (2013). Time and space distribution of coseismic slip of the 2011 Tohoku earthquake as inferred from tsunami waveform data. *Bulletin of the Seismological Society of America*, *103*(2B), 1473–1492. https://doi.org/10.1785/0120120122
Sato, R. (1971). Crustal deformation due to dislocation in a multi-layered medium. *Journal of Physics of the Earth*, *19*(1), 31–46. https://doi.org/10.4294/jpe1952.19.31
Savage, J. (1987). Effect of crustal layering upon dislocation modeling. *Journal of Geophysical Research*, *92*(B10), 10,595–10,600. https://doi.org/10.1029/JB092iB10p10595
Savage, J. (1998). Displacement field for an edge dislocation in a layered half-space. *Journal of Geophysical Research*, *103*(B2), 2439–2446. https://doi.org/10.1029/97JB02562
Schmalzle, G. M., McCaffrey, R., & Creager, K. C. (2014). Central Cascadia Subduction Zone creep. *Geochemistry, Geophysics, Geosystems*, *15*, 1515–1532. https://doi.org/10.1002/2013GC005172
Shao, G., Li, X., Ji, C., & Maeda, T. (2011). Focal mechanism and slip history of the 2011 Mw 9.1 off the Pacific coast of Tohoku earthquake, constrained with teleseismic body and surface waves. *Earth, Planets and Space*, *63*(7), 9.
Simons, M., Minson, S. E., Sladen, A., Ortega, F., Jiang, J., Owen, S. E., et al. (2011). The 2011 magnitude 9.0 Tohoku-Oki earthquake: Mosaicking the megathrust from seconds to centuries. *Science*, *332*(6036), 1421–1425. https://doi.org/10.1126/science.1206731
Suito, H., Nishimura, T., Kobayashi, T., Ozawa, S., Tobita, M., & Imakiire, T. (2012). Co-and post-seismic deformation and fault model of the 2011 off the Pacific coast of Tohoku earthquake. *Zisin*, *2*(65), 95–121.
Synolakis, C. (2003). Tsunami and seiche. In *Earthquake engineering handbook* (pp. 9_1–9_90). Boca Raton, FL: CRC Press.
Tappin, D. R., Grilli, S. T., Harris, J. C., Geller, R. J., Masterlark, T., Kirby, J. T., et al. (2014). Did a submarine landslide contribute to the 2011 Tohoku tsunami? *Marine Geology*, *357*, 344–361. https://doi.org/10.1016/j.margeo.2014.09.043
Tassara, A., & Echaurren, A. (2012). Anatomy of the Andean subduction zone: Three-dimensional density model upgraded and compared against global-scale models. *Geophysical Journal International*, *189*(1), 161–168. https://doi.org/10.1111/j.1365-246X.2012.05397.x
Titov, V. V., & Gonzalez, F. (1997). Implementation and testing of the method of splitting tsunami (MOST) model, US Department of Commerce, National Oceanic and Atmospheric Administration, Environmental Research Laboratories, Pacific Marine Environmental Laboratory.
Titov, V. V., Mofjeld, H. O., González, F. I., & Newman, J. C. (1999). Offshore forecasting of Hawaiian tsunamis generated in Alaskan-Aleutian subduction zone. *NOAA Technical Memorandum ERL PMEL*, *114*, 22.
Trasatti, E., Kyriakopoulos, C., & Chini, M. (2011). Finite element inversion of DInSAR data from the Mw 6.3 L'Aquila earthquake, 2009 (Italy). *Geophysical Research Letters*, *38*, L08306. https://doi.org/10.1029/2011GL046714
Tung, S., & Masterlark, T. (2016). Coseismic slip distribution of the 2015 Mw7.8 Gorkha, Nepal, earthquake from joint inversion of GPS and InSAR data for slip within a 3-D heterogeneous Domain. *Journal of Geophysical Research: Solid Earth*, *121*, 3479–3503. https://doi.org/10.1002/2015JB012497
Tung, S., & Masterlark, T. (2018). Resolving source geometry of the August 24 2016 Amatrice, Central Italy earthquake from InSAR data and 3D finite element modeling, Bulletin of the Seismological Society of America, Accepted.
Ulutas, E. (2013). Comparison of the seafloor displacement from uniform and non-uniform slip models on tsunami simulation of the 2011 Tohoku-Oki earthquake. *Journal of Asian Earth Sciences*, *62*, 568–585. https://doi.org/10.1016/j.jseaes.2012.11.007
Uslu, B., Borrero, J. C., Dengler, L. A., & Synolakis, C. E. (2007). Tsunami inundation at Crescent City, California generated by earthquakes along the Cascadia Subduction Zone. *Geophysical Research Letters*, *34*, L20601. https://doi.org/10.1029/2007GL030188
Wang, H. F. (2000). *Theory of linear poroelasticity: With applications to geomechanics and hydrogeology*. Princeton, NJ: Princeton University Press.
Wang, X. (2008). Numerical modelling of surface and internal waves over shallow and intermediate water.
Wang, X., & Liu, L. (2006). An analysis of 2004 Sumatra earthquake fault plane mechanisms and Indian Ocean tsunami. *Journal of Hydraulic Research*, *44*(2), 147–154. https://doi.org/10.1080/00221686.2006.9521671
Wang, X., & Power, W. (2011). COMCOT: a tsunami generation propagation and run-up model.
Wang, R., Wells, S., Mazzotti, D., Hyndman, R. D., & Sagiya, T. (2003). A revised dislocation model of interseismic deformation of the Cascadia Subduction Zone. *Journal of Geophysical Research*, *108*(B1), 2026. https://doi.org/10.1029/2001JB001227
Wang, R., Lorenzo-Martín, F., & Roth, F. (2006). PSGRN/PSCMP—A new code for calculating co-and post-seismic deformation, geoid and gravity changes based on the viscoelastic-gravitational dislocation theory. *Computers & Geosciences*, *32*(4), 527–541. https://doi.org/10.1016/j.cageo.2005.08.006
Wei, Y., Newman, A. V., Hayes, G. P., Titov, V. V., & Tang, L. (2014). Tsunami forecast by joint inversion of real-time tsunami waveforms and seismic or GPS data: Application to the Tohoku 2011 tsunami. *Pure and Applied Geophysics*, *171*(12), 3281–3305. https://doi.org/10.1007/s00024-014-0777-z
Williams, C. A., & Wallace, L. M. (2015). Effects of material property variations on slip estimates for subduction interface slow-slip events. *Geophysical Research Letters*, *42*, 1113–1121. https://doi.org/10.1002/2014GL062505

Witter, R. C., Zhang, Y. J., Wang, K., Priest, G. R., Goldfinger, C., Stimely, L., et al. (2013). Simulated tsunami inundation for a range of Cascadia megathrust earthquake scenarios at Bandon, Oregon, USA. *Geosphere*, *9*(6), 1783–1803. https://doi.org/10.1130/GES00899.1

Xu, C., Liu, Y., Wen, Y., & Wang, R. (2010). Coseismic slip distribution of the 2008 Mw 7.9 Wenchuan earthquake from joint inversion of GPS and InSAR data. *Bulletin of the Seismological Society of America*, *100*(5B), 2736–2749. https://doi.org/10.1785/0120090253

Yamazaki, Y., Cheung, K. F., & Lay, T. (2013). Modeling of the 2011 Tohoku near-field tsunami from finite-fault inversion of seismic waves. *Bulletin of the Seismological Society of America*, *103*(2B), 1444–1455. https://doi.org/10.1785/0120120103

Yue, H., & Lay, T. (2011). Inversion of high-rate (1 sps) GPS data for rupture process of the 11 March 2011 Tohoku earthquake (Mw 9.1). *Geophysical Research Letters*, *38*, L00G09. https://doi.org/10.1029/2011GL048700